A Modular Framework for the Plausible Depiction of Starburst Patterns

by

Yuxiang Sun

A thesis
presented to the University of Waterloo
in fulfillment of the
thesis requirement for the degree of
Master of Mathematics
in
Computer Science

Waterloo, Ontario, Canada, 2025

Author's Declaration

I hereby declare that I am the sole author of this thesis. This is a true copy of the thesis, including any required final revisions, as accepted by my examiners.

I understand that my thesis may be made electronically available to the public.

Abstract

When human viewers look at an intense light source, they can observe a set of dense spikes radiating from its center. The observed spike patterns result from a complex optical process known as the starburst phenomenon. These patterns have been frequently depicted in virtual applications (e.g., films and video games) to enhance the perception of brightness. From a broader scientific perspective, they also have relevant real life implications such as the impairing of driving safety. This may occur when an observed starburst pattern saturates a driver's field of view. Previous computer graphics works on the simulation of the starburst phenomenon have primarily relied on the assumption that the resulting patterns are formed by light being obscured and diffracted by particles in the observer's eyeball during the focusing process. However, the key role played by background luminance on the perception of starburst patterns has been consistently overlooked. By also taking into account this pivotal factor as well as the different physiological characteristics of the human photoreceptor cells, we propose a modular framework capable of producing plausible visual depictions of starburst patterns for daytime and nighttime scenes. To enhance the physical correctness and resolution of the simulated patterns, its formulation was guided by the Rayleigh-Sommerfeld diffraction theory and implemented using the Chirp Z Transform, respectively. We also introduce a biophysically-inspired algorithm to enable the seamless incorporation of the resulting patterns onto computer-rendered scenes. Besides examining theoretical and practical aspects associated with the use of the proposed framework in realistic image synthesis, we also derive biophysical insights that may contribute to the current knowledge about the inner workings of the starburst phenomenon.

Acknowledgements

First and foremost, I am grateful for the support of my supervisor, Professor Gladimir Valerio Guimarães Baranoski. Without his open-mindedness, we would not have pursued this topic—one that neither of us had prior experience in at the time. Without his sophisticated foundation in computer graphics, this work would have remained at the stage of pattern reproduction, leaving the mechanism behind the phenomenon unaddressed. And without his guidance on presenting this research, this thesis would not have taken the form it does today.

I would also like to acknowledge the support of my lab colleagues—Petri Matthew Varsa, Scott Steinfield and Frank Fan, listed in the order they joined the group. Their presence and conversations have been a source of support throughout my graduate studies.

Finally, I appreciate the time and effort of my thesis reviewers, Professor Paulo Alencar and Professor Khuzaima Daudjee (listed alphabetically by last name), for their thoughtful evaluation of this work.

Dedication

As an existent, I am grateful to my parents for bringing me into this world and raising me.

Here, I once again thank Gladimir for being more than an academic supervisor—a true mentor in life. The same goes for Petri, Scott and Frank, who have been friends just as much as colleagues.

I also appreciate everyone who has shared their experiences and observations on glare, starbursts and astigmatism. Since these phenomena cannot be objectively captured, your discussions have provided valuable insights for this research.

I am thankful to all who have been part of my life, as well as to those who came before me, leaving behind an intangible heritage.

Lastly, I want to acknowledge resource-sharing entities like Blender, Sketchfab and Freepik. Without them, creating illustrative images on my own would have been far more difficult.

May everyone have bright stars in their eyes, and may their light be seen—like stars in the night sky, shining with their own starburst.

Table of Contents

List of Figures

List of Tables

List of Abbreviations

CZT Chirp Z Transform xii, xv, 3, 12, 18, 22, 30–32, 35, 48

FFT Fast Fourier Transform xii, xv, 12, 22, 30–33, 48

HDR High Dynamic Range 4

HVS Human Vision System 1–3, 6, 9, 14, 15, 48, 58, 60

iFFT inerse Fast Fourier Transform 32

L Long (wavelength(s)) 13

LDR Low Dynamic Range 4

LED Light-Emitting Diode xii, 36, 37

M Medium (wavelength(s)) 13

PSF Point Spread Function 1, 2, 15, 17, 18, 24, 35, 37, 47

RGCs Retinal Ganglion Cells 7, 8

RS Rayleigh-Sommerfeld xi, 3, 9, 10, 18, 22, 24, 26–28, 30, 33, 35, 48

S Short (wavelength(s)) 13

SPD Spectral Power Distribution xii, 35–37

TVI Threshold Versus Intensity x, 14, 20, 21

Abridged List of Symbols

B Brightness level 20

k_{cone} Efficiency of cones 21

k_{rod} Efficiency of rods 21

L_v^{env} Stimulus from environment 21

f Focal length (m) 11, 16

$\mathcal{F}, \mathcal{F}^{-1}$ Fourier transform and its inverse 10

$V(\lambda)$ Photopic luminous efficiency function 20, 22

(x_i, y_i, z_i) Position on image (retina) plane 9

$(x_p, y_p, z_p = 0)$ Position on pupil plane 9

d Light propagation distance $(z_i - z_p)$ (m) 16

$P(x, y)$ Pupil or obstacle at position (x, y) 10

$M_{rel}(\lambda)$ Relative spectral power distribution 20

L_e Radiance $(W \cdot sr^{-1} \cdot m^{-2})$ 19, 20

a Radius of a circular aperture (m) 10, 11

$L_v^{refBlack}$ Stimulus for reference black 21

$L_v^{refWhite}$ Stimulus for reference white 21

$V'(\lambda)$ Scotopic luminous efficiency function 20, 22

$U(x, y, z)$ Complex amplitude at position (x, y, z) 9, 19

λ Wavelength (nm) 10

k Wave vector, $|k| = \frac{2\pi}{\lambda}$ 10

$f/\#$ F-number of an optical system 11

j Imaginary unit 10

N Number of rows of a square matrix 31

Chapter 1

Introduction

The stylized representations of stars usually contain multiple spikes that emanate from a bright spot. In real life, these spikes result from the diffraction of light waves in the imaging system [21]. Although the structure of the eyeball is different from that of a camera, the human visual system (HVS) is also affected by the diffraction during imaging. The pattern observed from an intense light source by the human eye consists of hundreds of dense spikes radiating from the source as illustrated in Fig. 1.1.

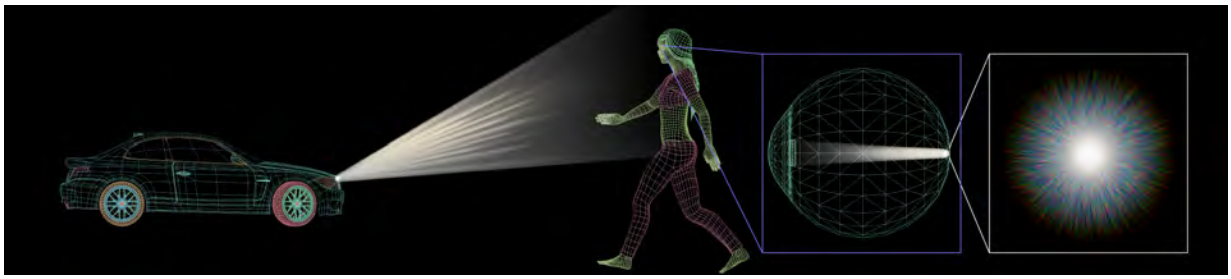

Figure 1.1: A night scene (rendered in wireframe mode) illustrating the occurrence of the starburst phenomenon. Since the luminous intensity of the car headlight is markedly stronger than its background, the observer sees a pattern consisting of a set of dense spikes radiating from the center of the light source. This pattern is elicited by a diffraction phenomenon happening inside the observer's eyeball.

The point spread function (PSF) can be employed to describe how the light from a point light source is distributed (spread) across the retina [36, 43, 49]. Accordingly, it has

been used to quantitatively characterize the starburst pattern in previous related works [23, 36, 43, 45].

The mechanism behind the starburst phenomenon is very complex and brings mixed usage of terminology. Some works use the term starburst [38, 47, 48] or ciliary corona [42, 45] to visually describe the phenomenon. Others broadly use the word glare [18, 36, 43] since such a pattern is only observed around bright light sources and impairs vision. Readers interested in further details may refer to the classification of glare phenomenon by Mainster et al. [24].

In this thesis, the expression starburst pattern is employed in connection with the process by which the optical structure of the human eye causes a pattern similar to the one depicted in Fig. 1.1, which is quantitatively described by the PSF. The term starburst phenomenon, on the other hand, refers to the observable event in which an average human observer perceives the aforementioned pattern around a bright light source. The use of the term "phenomenon" takes into account additional factors, such as background illumination and the light intensity threshold of the photoreceptor cells[1], distinguishing it from the use of the term "pattern." The significance of these aspects will be discussed in Chapter 6. Additionally, it is worth noting that human observers may also perceive other visual effects, such as halos and blooms, around bright light sources. Their simulation, however, is beyond the scope of this work.

Driving is a classic scenario for the starburst phenomenon to happen. Around noon, a driver may observe the pattern on a bright spot on the windows and chassis of other cars on the road. The specular reflection of sunlight induces this bright spot and can be classified as a secondary light source. In the nighttime, a driver may observe such a pattern from a streetlight or a headlight of an oncoming car as illustrated in Fig. 1.1. The starburst phenomenon affects driving safety by over-exposing and reducing the contrast of the environment.

It is intricate to reproduce the starburst phenomenon using traditional computer graphics techniques based on geometric (ray) optics since the pattern formed by hundreds of spikes results from diffraction, a wave optics phenomenon that can be associated with a high spatial frequency [11]. Moreover, the phenomenon occurs instantaneously and, thus, has also a high temporal frequency. This aspect challenges the HVS adaptation to light intensity variations, notably in driving situations [12], and makes the design of biophysically-based algorithms difficult.

Relevant efforts have been devoted to the study of the starburst phenomenon in computer graphics and related fields [18, 23, 27, 36, 37, 41, 43, 45]. However, the focus of

[1]Cells on the retina that respond to impinging light [9]. More details are provided in Chapter 3.

previous works has been on the shape of the pattern, overlooking background illumination and the physiological characteristics of the photoreceptor cells which also affect the phenomenon [24]. A notable exception is the work of Spencer et al. [43] which, to some extent, accounted for the role of the photoreceptor cells.

To propose a plausible modular framework for reproducing the starburst phenomenon, we build upon algorithms proposed by previous works while considering more closely the role played by the HVS. The proposed framework comprises two main stages, henceforth referred to as propagation and response stages. The former simulates the light travelling from the front of the eyeball to the retina, while the latter computes the retina response elicited by the light stimulus.

In the propagation stage, we employ the Rayleigh-Sommerfeld (RS) diffraction theory (with Ochoa's approximation) [40] to enhance the physical correctness of the simulated patterns and the Chirp Z transform (CZT) [13] to increase their resolution. In the response stage, we introduce a biophysically-inspired algorithm, based on the work of Ferwerda et al. [9], to convert luminance[2] to brightness[3].

The remainder of this thesis is organized as follows. In Chapter 2, we briefly examine previous works in related areas. In Chapter 3, we concisely review biophysical aspects and methodologies relevant to this research. In Chapter 4, we describe the proposed framework and implementation aspects. In Chapter 5, we assess theoretical aspects associated with the propagation stage. In Chapter 6, we present our simulation results obtained through the response stage and discuss the plausibility and applicability of the proposed framework. In Chapter 7, we outline biophysical insights derived from our simulations. Finally, in Chapter 8, we conclude the thesis and indicate directions for future investigations in this area.

[2]Luminance is a quantity used to describe the light intensity and it is measured in candelas per square meter [4]. More details are provided in Chapter 3.

[3]Brightness corresponds to an aspect of visual perception whereby an area (or light source) appears to emit more or less light [1].

Chapter 2

Related Work

In the 1950s, Simpson [42] observed coloured rings around lamps similar to atmospheric phenomena such as haloes and coronas. He classified the patterns into three categories: lenticular halo, Descartes corona and ciliary corona (called starburst in this thesis). Through detailed observations, he also speculated that the starburst patterns are caused by a uniform distribution of particles in the eye. Since then, these patterns have attracted the attention of researchers from different fields, including computer graphics.

In the 1990s, the glare phenomena (which includes starburst) and high dynamic range (HDR) were often associated with each other [43]. Glare originates from bright light sources [36]. Accordingly, large ranges of illumination intensity are required to render them properly. The dynamic range of an image is usually computed by dividing its brightest pixel by its darkest pixel. The ratio for traditional low dynamic range (LDR) images is usually $256:1$, while HDR images have a significantly larger ratio (*e.g.*, $10^6:1$) [4]. Besides the use of tone mapping[1] techniques to map one set of colours to another to approximate the appearance of HDR images, one can apply glare to an LDR image to give the audience an HDR perception of a given scene [36].

2.1 Pattern Reproduction

Shinya et al. [41] used star-like lines to increase perceived brightness when rendering transparent objects. They analyzed the structure of the "cross-screen filter" used by pho-

[1] Tone mapping is an operation that compresses the range of illumination intensities of an image while preserving information like contrast and colour appearance [4].

tographers, and used it to generate patterns similar to those captured by the cameras. When Nakamae et al. [27] simulated driving at night, they accounted for the diffraction pattern produced by street lights due to eyelashes. Rokita [37] claimed that Nakamae's simulations [27] did not take into account the internal structure of the eye, and proposed an algorithm based on Simpson's observations [42]. His improved algorithm produced rendering results that more closely approximated what humans observe rather than what cameras capture.

Spencer et al. [43] systematically summarized the structure of the eyeball and proposed a method of generating glare accordingly. Compared to the previous works, their method pioneered the incorporation of physiological factors in glare simulation. They took into account two types of photoreceptor cells: cones and rods (Section 3.1).

Kakimoto et al. [18] proposed the use of Fourier optics (wave optics) for simulating glare patterns. They believed that the pattern is the result of the Fraunhofer diffraction[2] of light at given apertures or obstacles. Their work only considered the shape of eyelashes and pupils, not the lens fiber or particles in the eyeball. Subsequently, van den Berg et al. [45] were the first to simulate the pattern based on particles in an eyeball. Their results have significantly denser spikes compared to the previous results mentioned earlier [18, 27, 37, 41, 43]. Ritschel et al. [36] combined previous works [18, 45] and used Fourier optics to simulate particles in the eyeball while also adding a temporal factor. Luidolt et al. [23] brought the application of glare to virtual reality while incorporating the colour shift due to night vision and visual acuity reduction in their simulations.

2.2 Human Visual System and Tone Mapping

In terms of luminance range, the human eye detects from 10^{-6} to 10^{+8} Nits (units of candela per square meter [4]), a full 14 orders of magnitude [9]. In order to display what our eyes can see (especially details or high-frequency signals) on LDR screens, one can employ tone mapping algorithms. Some of them are biologically-based and others are not. Here, we briefly comment on three seminal papers on this topic. The reader interested in more details about tone mapping is referred to the work of Banterle et al. [4].

In 1993, Tumblin et al. [44] proposed a mapping based on subjective brightness. When a person perceives the same brightness in the real world and on the monitor, the mapping is established via the corresponding luminance. However, this method reduces the visibility

[2]An approximation for far-field diffraction where wave propagation is described by a single Fourier transform [11]. More details are given in Chapter 3.

of dark areas. In the following year, Ward [46] proposed a contrast-based algorithm that preserves visibility. Afterwards, Ferwerda et al. [9] investigated the structure of the HVS and improved the contrast-based algorithm.

Chapter 3

Biophysical Background

In this chapter, we provide a concise overview of biophysical concepts and mathematical methods relevant to the development of the proposed framework described in Chapter 4.

3.1 Optical Structure of the Human Eye

The eye components directly related to optical imaging and perception include the cornea, aqueous humour, iris (pupil), lens, vitreous body and retina as shown in Fig. 3.1.

The function of the cornea and lens is to focus incoming light onto the retina. However, these components of the human eye's optical structure cannot focus parallel incident light rays onto a single point. This limitation is called optical aberration [29]. Some of the most noticeable types of aberration are defocus (myopia and hyperopia), primary astigmatism, primary spherical aberration and primary coma [29].

The iris can expand and contract to change the size of the pupil to control the amount of light entering the eye. The pupil's diameter ranges from 2 to 7 mm depending on the intensity of the ambient light at the time [9].

According to van den Berg et al. [45], there are many evenly distributed particles in the cornea, lens and vitreous body, which supports Simpson's speculation [42] mentioned in Chapter 2. The reader interested in more details about the obstacles in the eyeball is referred to the work of Ritschel et al. [36].

There are three types of photoreceptor cells on the retina: rods, cones and retinal ganglion cells (RGCs). Among them, cones and rods can absorb photons and generate

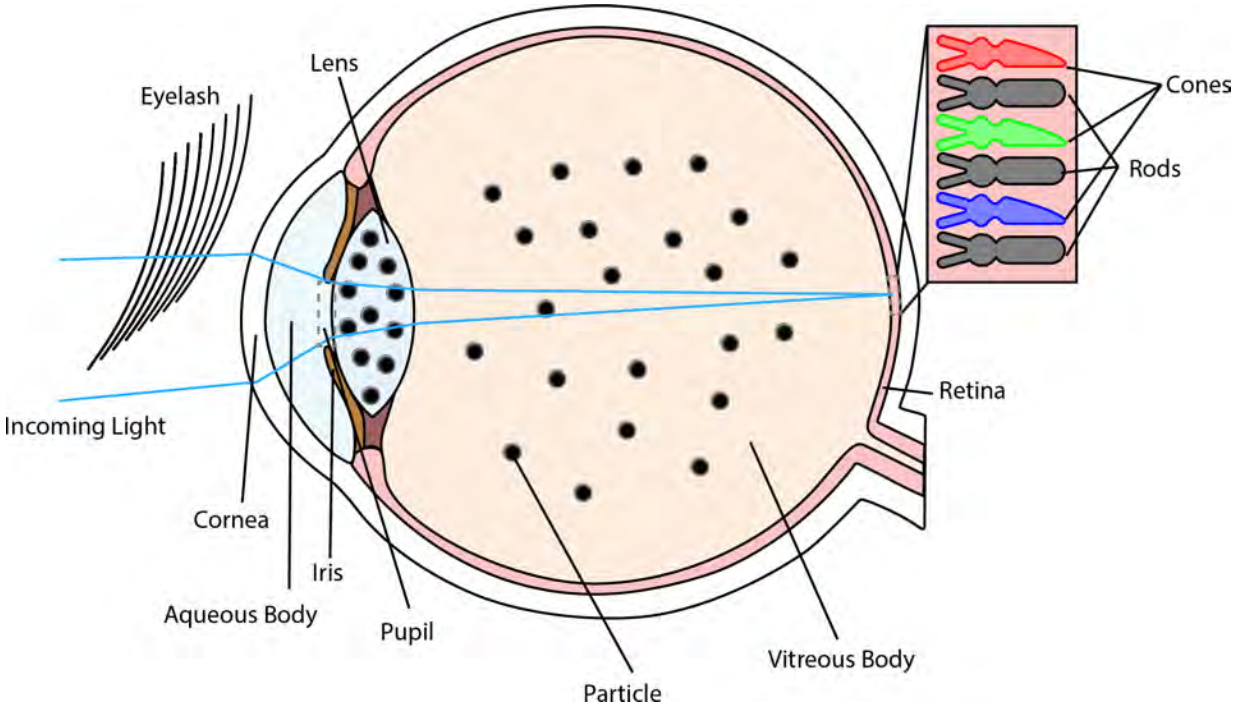

Figure 3.1: Sketch illustrating the anatomical structure of the eye. Incoming light reaches the retina often being refracted by the cornea and lens. It then stimulates the photoreceptor cells (cones and rods) on the retina. As light propagates toward the eyeball, its path may be affected by the presence of eyelashes, the iridal microstructure and particles distributed on the lens and intravitreous body of the eyeball.

electrical signals. The cones are mainly responsible for daytime vision, while the rods are mainly responsible for nighttime vision. The RGCs are responsible for the coordination of physiological responses, such as pupil constriction [34], which are outside the scope of this work.

3.2 Radiometric and Photometric Quantities

Radiance and irradiance, originally from radiometry, are common quantities employed in computer graphics. Radiance corresponds to the irradiance (radiant power of light incident on a surface divided by its area) per solid angle. This quantity (expressed in steradians), in turn, refers to the directions from which light is incident on the surface [10]. Accordingly,

radiance and irradiance are expressed in units of watts per square meter and watts per steradian per square meter, respectively [10].

Luminance, employed in photometry, takes into account the characteristics of the HVS [4]. It can be obtained from radiance by weighting with spectral response from a standard observer, and it is expressed in Nits [4]. While these three quantities are objective and measurable, brightness refers to the subjective sensation produced by light [44].

3.3 Scalar Diffraction Theory

Geometric optics formulation is unsuitable for correctly handling the light propagation in the eyeball since the microstructures (*e.g.*, particles and fibers) in the eye can cause diffraction (wave optics) effects [36]. This section briefly introduces wave optics concepts required to properly account for those effects.

As an electromagnetic wave, light has two components: an electric field and a magnetic field. They are coupled through Maxwell's equations [11]. A reliable approximation can be obtained by treating the oscillation of the wave as a scalar as long as the diffracting structures are large compared to the wavelength of light [11]. Assuming, as previous studies have done [23, 36], that the relevant eye structures are considerably larger than the wavelength of visible light, then the above condition holds. Accordingly, we treated light oscillation as a scalar quantity in this work (*i.e.*, neglecting polarization [11]). We note that this simplification does not conflict with representing the distribution of light waves on a plane screen using a matrix.

3.3.1 Rayleigh-Sommerfeld Diffraction Theory

Under the scalar diffraction theory and finite aperture boundary conditions (*i.e.*, a finite aperture size), the Rayleigh-Sommerfeld (RS) diffraction solution provides an approximate monochromatic solution to Maxwell's equations, which can be expressed as [11]:

$$U(x_i, y_i, z_i) = \frac{z_i}{2\pi} \iint_P U(x_p, y_p, 0)(\frac{1}{r} - jk)\frac{e^{jkr}}{r^2} dx_p dy_p, \tag{3.1a}$$

$$r = \sqrt{z_i^2 + (x_i - x_p)^2 + (y_i - y_p)^2}, \tag{3.1b}$$

where $(x_p, y_p, z_p = 0)$ and (x_i, y_i, z_i) are points on the pupil plane and image plane, respectively, $U(x, y, z)$ is the complex amplitude that encodes the amplitude and phase of a wave

at a specific point, λ is the wavelength, $k = \frac{2\pi}{\lambda}$ is the wave vector and $P(x, y)$ is the mask representation of pupil or obstacle at position (x, y). We note that j is used to represent the imaginary unit.

The RS diffraction integral can be solved through the convolution theorem (Eq. 3.2), which states that the Fourier transform of the convolution of two functions is the product of their Fourier transform [11]:

$$\mathcal{F}[\iint u(x,y)v(x-\xi,y-\eta)dxdy] = \mathcal{F}[u(x,y)]\mathcal{F}[v(x,y)], \tag{3.2}$$

where $\mathcal{F}, \mathcal{F}^{-1}$ are the Fourier transform and its inverse. By defining u and v as:

$$u(x_p, y_p, z_p) = U(x_p, y_p, z_p), \tag{3.3a}$$

$$v(x_i, y_i, z_i) = \frac{z_i}{2\pi}(\frac{1}{r} - jk)\frac{e^{jkr}}{r^2}, r = \sqrt{z_i^2 + x_i^2 + y_i^2}, \tag{3.3b}$$

the integral part of RS (Eq. 3.1) could be written as a convolution:

$$U(x_i, y_i, z_i) = \mathcal{F}^{-1}(\mathcal{F}(u)\mathcal{F}(v)). \tag{3.4}$$

Although the convolution solution expressed in Eq. 3.4 is accurate, it is computationally expensive as we will show in Section 5.7. Thus, multiple diffraction approximations exist based on the light propagation distance. In the remainder of this section, we will briefly review some of these approximations relevant to our simulations.

3.3.2 Ochoa's Approximation

Ochoa [30] proposes that, for circular apertures, the distance r (Eq.3.1b) can be approximated as:

$$r \approx \sqrt{x_p^2 + y_p^2 + z^2} - \frac{x_i x_p + y_i y_p}{A_z}, \tag{3.5a}$$

$$A_z = \frac{3a^4}{4\sqrt{a^2+z^2} - 12z^2\sqrt{a^2+z^2} + 8z^3}, \tag{3.5b}$$

where a represents the radius of the aperture.

The Ochoa's approximation can be obtained by substituting Eqs. 3.5a and 3.5b into the exponential term (e^{jkr}) of Eq. 3.1, and replacing r by $r_n = \sqrt{x_p^2 + y_p^2 + z^2}$ in the

denominators of Eq. 3.1a:

$$\begin{aligned} U(x_i, y_i, z_i) =& \frac{z_i}{2\pi} \iint_P [U(x_p, y_p, 0)(jk - \frac{1}{r_n}) \frac{e^{jkr_n}}{r_n^2}] \\ & \times e^{-j\frac{2\pi}{\lambda A_z}(x_i x_p + y_i y_p)} dx_p dy_p \\ =& \frac{z_i}{2\pi} \mathcal{F}[U(x_p, y_p, 0)(jk - \frac{1}{r_n}) \frac{e^{jkr_n}}{r_n^2}]. \end{aligned} \tag{3.6}$$

The error of this approximation decreases as the f-number ($f/\#$) of the optical system increases [30]. This parameter is expressed as:

$$f/\# = \frac{f}{2a}, \tag{3.7}$$

where f and a respectively represent the focal length and the radius of the circular aperture causing diffraction.

3.3.3 Fresnel Approximation

If $r \gg \lambda$, Eq. 3.1a can be simplified as [11]:

$$U(x_i, y_i, z_i) = \frac{z_i}{j\lambda} \iint_P U(x_p, y_p, 0) \frac{e^{jkr}}{r^2} dx_p dy_p. \tag{3.8}$$

When the propagation distance d satisfies the condition:

$$d \gg \sqrt[3]{\frac{\pi}{4\lambda}[(x_i - x_p)^2 + (y_i - y_p)^2]^2_{max}}, \tag{3.9}$$

where max refers to the maximum possible expression value given any valid (x_i, y_i, x_p, y_p), the parameter r (Eq. 3.1b) can be approximated by:

$$r \approx d[1 + \frac{1}{2}(\frac{x_i - x_p}{d})^2 + \frac{1}{2}(\frac{y_i - y_p}{d})^2]. \tag{3.10}$$

The Fresnel approximation can then be obtained by plugging Eq. 3.10 into Eq. 3.8 [11]:

$$\begin{aligned} U(x_i, y_i, z_i) =& \frac{e^{jkz_i}}{j\lambda z_i} e^{j\frac{k}{2z_i}(x_i^2+y_i^2)} \iint_P [U(x_p, y_p, 0) e^{j\frac{k}{2z_i}(x_p^2+y_p^2)}] \\ & \times e^{-j\frac{2\pi}{\lambda z_i}(x_i x_p + y_i y_p)} dx_p dy_p \\ =& \frac{e^{jkz_i}}{j\lambda z_i} e^{j\frac{k}{2z_i}(x_i^2+y_i^2)} \mathcal{F}[U(x_p, y_p, 0) e^{j\frac{k}{2z_i}(x_p^2+y_p^2)}]. \end{aligned} \tag{3.11}$$

We note that the Fresnel approximation was adopted by Ritschel et al. [36] to reproduce glare.

3.3.4 Fraunhofer Approximation

If $z_i \gg \frac{k(x_p^2+y_p^2)_{max}}{2}$, then $e^{j\frac{k}{2z_i}(x_p^2+y_p^2)}$ approaches to 1. The Fraunhofer approximation can be obtained by removing the exponential term inside the Fourier transform of the Fresnel approximation (Eq. 3.11) [11]:

$$U(x_i, y_i, z_i) = \frac{e^{jkz_i}}{j\lambda z_i} e^{j\frac{k}{2z_i}(x_i^2+y_i^2)} \mathcal{F}[U(x_p, y_p, 0)]. \tag{3.12}$$

We also note that the Fraunhofer approximation has been adopted by Kakimoto et al. [18] to reproduce the glare.

3.3.5 Chirp Z Transform

The computation of Fourier transforms can be more efficiently carried out using the Fast Fourier transform (FFT) [11]. A generalized version of the FFT, called Chirp Z transform (CZT) [5], allows for more flexibility in the selection of a region of interest in frequency space [13]. Accordingly, one can directly generate the pattern on the image plane within the region of interest without having to scale it or crop it afterwards.

3.4 Visual Adaptation

Besides diffraction, human visual adaptation is also relevant to the perception of the starburst phenomenon. In this section, we concisely review some relevant properties of cones

and rods that are taken into account in our work. The reader interested in more information about them is referred to the work of Ferwerda et al. [9].

3.4.1 Cones and Rods

There are three types of cones that are sensitive to long (L), medium (M) and short (S) in the visible spectrum, respectively. There is only one type of rod, however. Therefore, the cones are directly associated with the perception of colour (chromatic vision), while the rods are not (achromatic vision) [9]. Colour spaces, such as LMS, were developed taking these aspects into consideration [4].

3.4.2 High Dynamic Range

Cones and rods collaborate to provide humans vision with a dynamic range that can be divided into scotopic (10^{-6} to 10^{-2} Nits), mesopic (10^{-2} to 10^{1} Nits) and photopic (10^{1} to 10^{8} Nits). Rods are quite sensitive to light and provide achromatic vision at the scotopic level of illumination. Cones are less sensitive than rods, providing chromatic vision at the photopic level of illumination. Both types of cells contribute to vision under mesopic illumination. We note that the diffraction pattern also has a distinctly high dynamic range in terms of luminance distribution (Section 5.5).

3.4.3 Non-linear Perception and Stimulus Threshold

Human vision follows Weber-Fechner's law [3]. It states that an additional physical stimulus (*e.g.*, light) needs to surpass a certain threshold to make humans notice its existence, and such a threshold is proportional to the logarithm of existing stimulus [3]. Ferwerda et al. [9] investigated the relationship between this threshold and background luminance (Fig. 3.2) and proposed a tone mapping operator based on that.

3.4.4 Photo-sensitivity and Bleaching

The sensitivity of cones and rods is strongly affected by rapid changes in the illumination of an environment. According to Ferwerda et al. [9], when the environment suddenly becomes bright, rods restore 80% of their photo-sensitivity in two seconds, while it takes 10 minutes

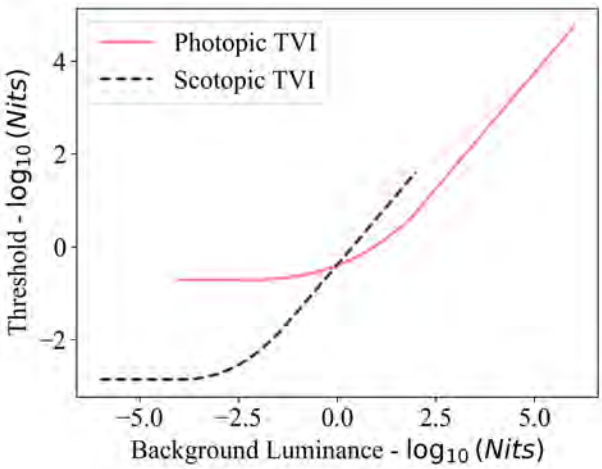

Figure 3.2: Graph depicting threshold versus intensity (TVI) values as a function of background luminance [9]. It indicates the luminance threshold that needs to be surpassed so that a person can perceive that there is an increment of brightness considering a given background luminance. The photopic TVI values refer to cones, while the scotopic TVI values refer to rods.

for the cones to fully restore their sensitivity. Besides, rods lose their effectiveness in very bright conditions, a phenomenon called bleaching [9].

We note the HVS, especially the component of converting light signals to electrical signals (a.k.a visual phototransduction), is much more complex than the concise description provided in this section. In fact, the coordination mechanism between cones and rods in the mesopic level of illumination is still not completely understood [12].

Chapter 4

Proposed Framework

We simulate the starburst phenomenon by decomposing its eliciting process into two stages, namely, propagation and response. These are schematically illustrated in Fig. 4.1.

In the propagation stage, we model how the light enters the eyeball and induces a stimulus on the retina with a starburst pattern that is quantitively described by the PSF. We note that this has already been accomplished by previous works [18, 36]. We expand on that by introducing aberration to the lens and employing the wave propagation methods mentioned in Section 3.3.1 and Section 3.3.2.

In the response stage, we model how the stimulus from light is processed by photoreceptor cells. We propose a biophysically-inspired algorithm that converts the radiance field on the retina into a brightness level. The algorithm accounts for the specific characteristics of the HVS introduced in Section 3.4.

4.1 Simulation Setup

The propagation stage includes the modelling of the light source, lens, pupil, obstacles and retina. In the context of wave optics, the light wave on the pupil plane (*i.e.*, the light emitted by the source that reaches the pupil plane) is represented by its complex amplitude. The lens is then represented by a phase transformation that modifies the phase of this wave [11] as represented in Fig. 4.2. Additionally, pupils and obstacles are represented as masks on the pupil plane. The light wave on the image plane is also represented by its complex amplitude, and it is expected to be computed based on the propagation of light waves from the pupil plane.

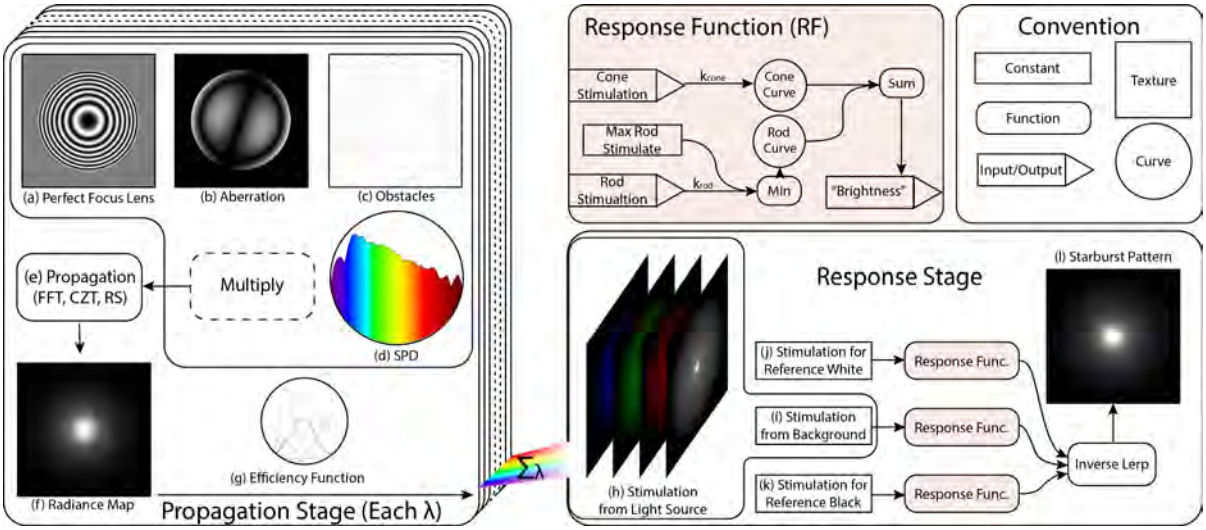

Figure 4.1: Overview of the modular framework proposed for the plausible reproduction of the starburst phenomenon. A parallel incoming light, represented by a spectral power distribution (d), is converged considering a perfect focus lens (a), aberration (b) and obstacles (c). The propagation (e) of the light wave is occluded by obstacles in the eyeball (*e.g.*, particles) (c) and leads to diffraction. The propagation results on the retina are converted to a radiance map (f) and further converted to luminance by multiplying with the efficiency (g) associated with the photoreceptor cells on the retina and the respective wavelengths. The propagation stage evaluates each wavelength and the results are accumulated to obtain the stimulus on the retina from the light source (h). A uniform background luminance is added to the stimulus. The response function is then applied to (i + h) to produce brightness. By applying inverse linear interpolation (Lerp), with the brightness of reference white (j) and reference black (k), the final result is obtained (l).

Aligned with previous works [18, 36], we set the lens at the origin, with the z-axis as the optics axis. We also set the retina plane to be $z = d$, where d is the propagation distance. The light source is a plane wave (*i.e.*, directional light) parallel to the eye axis, and the lens can achieve perfect focus (*i.e.*, $d = f$ where f is focal length and no aberration). With the above setting, we can define the light source and perfect focus lens using the following expressions:

$$U_0(x_p, y_p, z_p = 0) = A \cdot e^{-j \cdot k \cdot z_p}, \tag{4.1a}$$

$$t_{lens}(x, y) = e^{-j\frac{k}{2f}(x^2+y^2)}, \tag{4.1b}$$

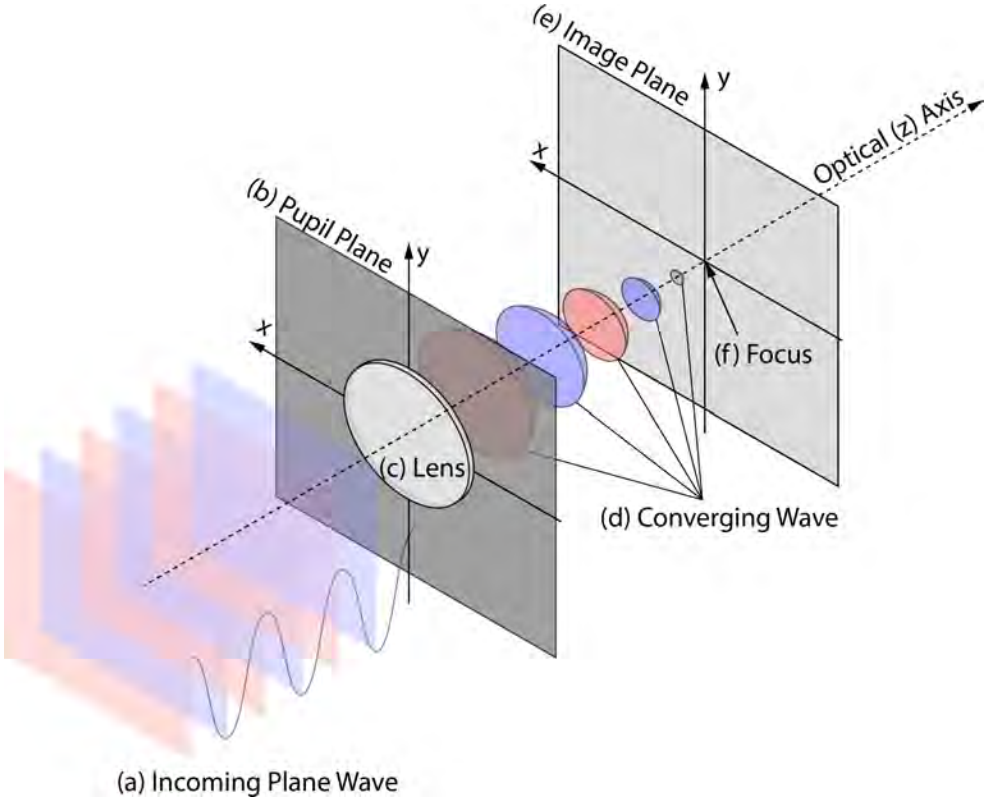

Figure 4.2: Sketch illustrating the main steps of wave propagation modelling employed in this work. The incoming plane wave (a) is converged (d) by the focus lens (c) on the pupil plane (b). It then propagates to the focus (f) on the image plane (e).

where A is the amplitude of a wave. Note that we select directional light for convenience when calculating focal length. It can be converted to a point source with a lens with higher refractive power to better fit the PSF definition.

Based on anatomical data [2], and for simplicity, we set the distance from the center of the lens to the retina to be 20 mm and the refractive index of liquid in the eyeball to be 1.4.

Aberration is represented by phase transformation with Zernike polynomials [1] [29]. To add aberration to the lens, we multiply the phase transform of the former by the phase transform of the latter (Eq. 4.1b).

[1] A set of orthogonal polynomials defined on the unit disk [29]. They are extensively used to describe aberrations [29].

4.2 Propagation Stage

Based on the setup schematically presented in Fig. 4.2, we can calculate the light wave (represented by complex amplitude) at the retina (image plane) by applying any of the propagation methods introduced in Section 3.3 to the light wave on the pupil plane: RS diffraction (Eq. 3.1), Ochoa's approximation of RS (Eq. 3.5), Fresnel approximation (Eq. 3.11) and Fraunhofer approximation (Eq. 3.12). We will begin by examining the Fresnel and Fraunhofer approximation used in previous works and then elaborate on the usage of CZT (Section 3.3.5) to increase the visual quality.

4.2.1 Fresnel and Fraunhofer Approximation

Kakimoto et al. [18] proposed that the light wave on the image plane can be obtained by applying Fraunhofer diffraction on a given pupil or obstacles (represented as a mask) on the pupil plane. Ritschel et al. [36] proposed the use of Fresnel diffraction to replace the former since it has higher physical accuracy. Considering the perfect focus setup described in Section. 4.1 (*i.e.*, $z_i = d = f$), by plugging Eq. 4.1b into Eq. 3.11, we obtain:

$$\begin{aligned} U(x_i, y_i, d) &\propto \mathcal{F}[U(x_p, y_p, 0) e^{j\frac{k}{2z_i}(x_p^2+y_p^2)}] \\ &= \mathcal{F}[U_0(x_p, y_p, 0) \cdot P(x_p, y_p) \cdot t(x_p, y_p) e^{j\frac{k}{2z_i}(x_p^2+y_p^2)}] \\ &= \mathcal{F}[U_0(x_p, y_p, 0) \cdot P(x_p, y_p) e^{j\frac{k-k}{2f}(x_p^2+y_p^2)}] \\ &= \mathcal{F}[U_0(x_p, y_p, 0) \cdot P(x_p, y_p)]. \end{aligned} \tag{4.2}$$

Eq. 4.2 shows that the PSF generated using the Fresnel approximation with perfect focused lens setup is equivalent to the PSF generated using the Fraunhofer approximation with the lens removed as indicated by Goodman et al. [11]. Therefore, we will treat these two approximations as the same propagation method and refer to them as "Fresnel approximation" for the remainder of this thesis.

4.2.2 Visual Resolution Improvement

Besides increasing physical accuracy, we could also improve the visual resolution of the simulation results (image). We can achieve that by implementing the Fourier Transform using CZT (Section 5.3). We remark that CZT enables users to manually select the region they are interested in (*i.e.*, zoom in).

4.2.3 Complex Amplitude to Radiance Conversion

Recall that radiance (L_e) corresponds to irradiance per solid angle (Chapter 3.2). The complex amplitude ($U(x, y, z)$) at the image plane needs to be converted to radiance to support rendering calculations. We know that irradiance is proportional to the modulo of complex amplitude [11]. We also assume that the solid angle [10] connecting the points on the lens and the pixels have approximately the same magnitude, *i.e.*, any small difference can be considered negligible. Accordingly, we employ the following conversion expression:

$$L_e = c_u |U|^2, \tag{4.3}$$

where the constant c_u is a user-defined parameter based on the choice of light source intensity (*e.g.,* bright or dim).

4.3 Response Stage

The stimulus that the light wave induces on the retina is not directly equivalent to what humans perceive. Besides that, the dynamic range of the radiance map (and the following luminance map), as we will discuss in Section 5.5, is too wide, which makes it impossible to add to the scene directly and display on the monitor. Considering this scenario, it seems logical to employ a tone mapping algorithm that can compress the dynamic range of the image while preserving information like contrast and colour appearance. However, a different approach may be appropriate when one takes into account the aspects outlined below.

We believe that background luminance should be regarded as an essential component of the starburst phenomenon. As pointed by Mainster et al. [24], the reduction of contrast caused by glare phenomena is more significant when the ratio between the light source luminance and the background luminance is larger. In other words, a glare phenomenon can be more easily perceived in dim backgrounds than in brighter ones.

We also remark that humans tend to ignore the details (specifically, contrast arising from subtle luminance variations) if the stimulus does not surpass the stimulus threshold as discussed in Section 3.4.3, which is the opposite of the goal of tone mapping, which aims to preserve details like contrast. Recall that the concept of tone mapping is borrowed from photography [44] to solve the dynamic range gap between the monitor and semiconductor sensor in the camera, not the gap between the former and ocular photoreceptor cells in the

eyeball. Although some tone mapping algorithms are guided by biological aspects, they still aim to preserve details.

Hence, we concluded that the response stage of the algorithm should allow some portions of the pattern to dissolve into the background since their luminous intensity may not reach the threshold (Section 3.4.3) required to enable their perception by human observers. Accordingly, we elected to develop a novel response function based on the observations and the measurements conducted by Ferwerda et al. [9].

4.3.1 Radiance to Luminance Mapping

After we calculate the radiance distribution (L_e) of the image plane (Section 4.2.3), we multiply it by the spectral power distribution ($M_{rel}(\lambda)$), spectral luminous efficiency ($V(\lambda)$ and $V'(\lambda)$), and integrate over all visible wavelengths to compute the photopic luminance:

$$L_v^{photopic} = \int_{360\ nm}^{830\ nm} V(\lambda) M_{rel}(\lambda) L_e(\lambda) d\lambda, \tag{4.4}$$

and the scotopic luminance:

$$L_v^{scotopic} = \int_{360\ nm}^{830\ nm} V'(\lambda) M_{rel}(\lambda) L_e(\lambda) d\lambda, \tag{4.5}$$

where $V(\lambda)$ and $V'(\lambda)$ are photopic and scotopic spectral luminous efficiencies, respectively. The spectral range ($360 - 830\ nm$) considered in Eqs. 4.4 and 4.5 corresponds to the spectral domain of the employed colour matching function and luminous efficiency curve, respectively [31]. Further information is provided in Section 4.5.

4.3.2 Luminance to Brightness Mapping

We build our mapping algorithm using the threshold versus intensity (TVI) curve (Fig. 3.2), which indicates the threshold of perception that needs to be surpassed so that a perception of increment in brightness can be elicited. Suppose that each brightness increment is identical, then at any given brightness level B, the required stimulus can be calculated

iteratively as:

$$L_v(B = 0) = 0; \tag{4.6a}$$

$$TVI(L_v(B = i)) = L_v(B = i + 1) - L_v(B = i); \tag{4.6b}$$

Eq. 4.6a is a trivial base case. It shows that if there is no illumination, the brightness is 0, and vice versa. Eq. 4.6b conveys that if someone wants to have a brightness level incremental to level $i + 1$ from level i, the amount of luminance needed is given by TVI curve evaluated at luminance with brightness level i which is $TVI(L_v(B = i))$. Since Eq. 4.6 is monotonically increasing, we could use its inverse function (L_v^{-1}) to build a mapping from luminance to brightness.

To simulate the bleaching effect of rods (Section 3.4.4), we set the upper bound of stimulus from rods to 10 Nits [9]. For the adaptation effect (Section 3.4.4), sensitivities, as user-defined parameters, are introduced as coefficients to the cone stimulus and rod stimulus, respectively. Lastly, the brightness level calculated from cones and rods is combined and expressed as:

$$B(L_v^p, L_v^s) = B^p(k_p \cdot L_v^p) + B^s(\min(k_s \cdot L_v^s, 10)), \tag{4.7}$$

where B^p and B^s are the inverse of Eq. 4.6 with photopic and scotopic TVI, respectively. Recall that cones are associated with scotopic illumination, while rods are associated with photopic illumination (Section 3.4.1). Accordingly, L_v^p and L_v^s respectively correspond to stimuli (expressed in terms of luminance) applied to these photoreceptor cells, with k_{cone} and k_{rod} representing their sensitivities (required for the simulation of the adaptation effect).

4.4 Background Luminance and Displaying Parameters

In addition to the light source, the background luminance also needs to be accounted for, and it is introduced by simply adding a new parameter L_v^{env} to the stimulus.

After mapping luminance to brightness using Eq. 4.7, the resulting brightness levels may still be outside 0 to 255 range (used to specify pixel colours). This problem is solved by defining the stimulus of black (0) and white (255) manually as $L_v^{refBlack}$ and $L_v^{refWhite}$. The final colour components are then calculated by applying inverse linear interpolation (Lerp)

and taking the brightness of the pattern, the brightness of the reference black and the brightness of the reference white as input values. This is accomplished using the following equation:

$$c_{LMS}[i] = \frac{B(L_v^p[i] + L_v^{env}[i], L_v^s[i] + L_v^{env}[i]) - B(L_v^{refBlack}[i], L_v^{refBlack}[i])}{B(L_v^{refWhite}[i], L_v^{refWhite}[i]) - B(L_v^{refBlack}[i], L_v^{refBlack}[i])}, \tag{4.8}$$

where LMS is the colour space that represents the response of three types of cones [4], with $i = 1, 2, 3$ representing each colour component. For the derivation of Eq. 4.8, please refer to Appendix A. The colour will then be converted to the RGB colour space via the multiplication with the transform matrix M_{RGB}^{LMS} [4]:

$$c_{RGB} = M_{RGB}^{LMS} \times c_{LMS}. \tag{4.9}$$

4.5 Implementation Aspects

The light wave, as a core component of the propagation stage, is represented as a square matrix of size $2^h \times 2^h$ for some integer h with a field complex number. The physical size assigned to the matrix that represents the pupil plane is $8\ mm \times 8\ mm$. Note that for the direct FFT implementations, we will double the physical size of the plane to $16\ mm \times 16\ mm$ for better visual results (padding with zeros the rows and columns that become empty once the pupil representation inside the square matrix is reduced). The value of h is chosen to meet the requirement of sampling (Section 5.1) or desired visual quality.

We implement each approximation algorithm with NumPy and Diffractio [39] library, which provides routines that implement the RS diffraction with convolution, CZT and Zernike polynomial. To facilitate visual interaction, we implement the response stage (Eqs. 4.7 to 4.10) in fragment shader with OpenGL [19] and adopt Dear ImGui [7] as the user interface.

For the choice of spectral luminous efficiencies, we adopt the CIE XYZ colour matching function for cones ($V(\lambda)$) (and convert to LMS colour space and RGB colour space afterwards) and CIE Scotopic luminosity curve for rods ($V'(\lambda)$) [31].

The propagation results are generated for each wavelength of the spectrum region from 360 to 830 nm, and stored in OpenEXR format [17]. Simulations are executed on a workstation with 128 GB RAM equipped with a 32-core Threadripper 3990x.

The mapping function (Eq. 4.6) is data-driven and discrete, which makes it difficult to invert and accommodate continuous input. To address these issues, we fit the data with

the following equation:

$$y(x) = k_a x + k_b \log(k_c + k_d e^{k_e x}) + k_f e^{-k_g^2 x} + k_h, \tag{4.10}$$

with the k parameters being assigned the values listed in Table. 4.1. We then plotted the fitted curve depicted in Fig. 4.3.

	Parameters							
Curve	k_a	k_b	k_c	k_d	k_e	k_f	k_g	k_h
Photopic	6.311	10.441	11.373	0.122	3.471	-9.058	0.566	-12.916
Scotopic	2.168	1.135	0.004	22.552	4.091	0.000	1.000	13.395

Table 4.1: Parameter values used to obtain the photopic and scotopic fitted curves depicted in Fig. 4.3

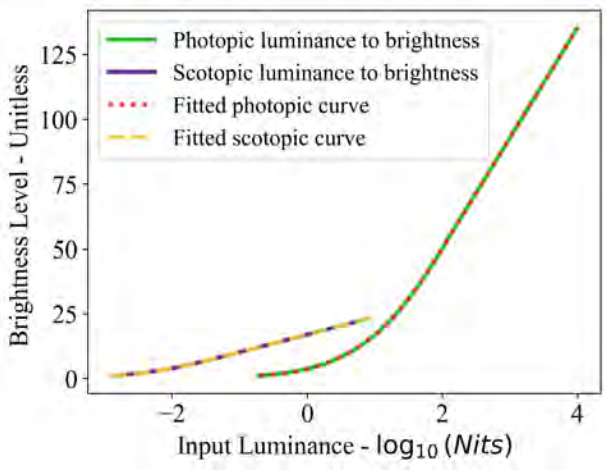

Figure 4.3: Fitted curves for luminance to brightness mapping function (inverse of Eq. 4.6). Two solid curves are data-driven functions for photopic and scotopic cases. The dotted curves are fitted results obtained using Eq. 4.10 and the parameter values listed in Table 4.1.

Chapter 5

Propagation Aspects

In Chapter 3, we introduced the Rayleigh-Sommerfeld (RS) diffraction theory as the solution for propagation under scalar diffraction theory, and mentioned its suitability for light propagation in the eyeball. In this chapter, each approximation method used in the propagation stage will be theoretically assessed by comparing its PSF to that provided by the RS solution.

5.1 Scene and Baseline

Under the eyeball scenario, we analyze each method by assigning:

- wavelength: $\lambda = 360\ nm$,
- physical size of plane: $\rho = (x_i - x_p)_{max} = (y_i - y_p)_{max} = 8\ mm$,
- propagation distance (also focal length): $z = f = 20\ mm$, and
- pupil radius: $a_{day} = 1\ mm$, $a_{night} = 3\ mm$.

Note that, although RS meets the theoretical conditions (Section 3.3), a reliable assessment still requires the sampling density to meet the Nyquist limit, which corresponds to the smallest sampling density required to completely recover a signal [11]. The required sampling rate is given by [40]:

$$\Delta\rho = \sqrt{\lambda^2 + \rho^2 + 2\lambda\sqrt{\rho^2 + d^2}} - \rho. \tag{5.1}$$

Considering the values assigned to λ, ρ and $d = f$, the size $(N \times N)$ of the square matrix representing the pupil plane needs to be at least $\rho/(\Delta\rho)$, which yields 11554.8096 in this case. This value further rounds up to 16384 since the Fast Fourier transform usually needs N to be a power of 2. Given this relatively large matrix size, a suitable approximation is necessary to manage potential computational costs.

5.2 Theoretical Soundness

In this section, we assess the theoretical soundness of each propagation approximation considered in this work. Although the failure to meet the conditions for an approximation suggests that the propagation result may be physically inaccurate, it may still lead to visual outcomes with a quality level suitable for computer graphics applications centred on the rendering of believable images [10].

5.2.1 Ochoa's approximation

Ochoa shows that the relative error monotonically decreases as the f number of the optical system increases [30]. The lower bound of f number in the eyeball setting is $f/\# = \frac{20\ mm}{2{\cdot}3\ mm} = 3.33$, while the relative error with $f/\# = 2$ is less than 0.25% from Ochoa's experiments [30]. Thus, with Ochoa's approximation, the relative error should be less than 0.25%.

5.2.2 Fresnel approximation

The distance requirement for Fresnel approximation can be directly calculated from Eq. 3.9. Plugging the selected values into Eq. 3.9 returns that the propagation distance needs to be far greater than 323.5 mm, which is far beyond the distance from the lens to the retina (around 20 mm). Thus, in theory, Fresnel diffraction cannot fully account for wave propagation in the eyeball. However, as indicated by Ritschel et al. [36], it can still be employed to produce believable patterns that can make computer-generated scenes appear brighter.

5.3 Airy Disk from Each Propagation Method

Single wavelength propagation with an ideal focus lens (*i.e.*, no aberration or particles) should produce an Airy disk [11]. We will assess the combination of each approximation of

propagation with the selected λ, ρ, z and f values mentioned in Section 5.1. For effective comparison, each pattern's energy is shifted to ensure that the centre intensities are the same for all patterns shown in this and the next section.

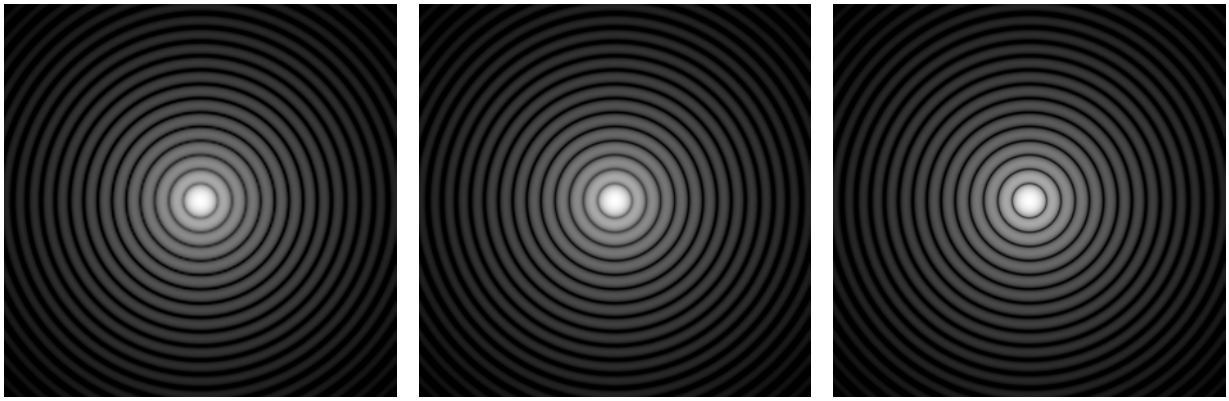

(a) (b) (c)

Figure 5.1: Airy patterns generated using different propagation algorithms and considering a 1 mm pupil radius. (a) Pattern obtained using Rayleigh-Sommerfeld (RS) diffraction solution. (b) Pattern obtained using Ochoa's approximation. (c) Pattern obtained using Fresnel approximation.

Fig. 5.1 presents images of Airy disks generated considering a 1 mm pupil radius. These images were generated using the RS diffraction solution (Fig. 5.1a), Ochoa's approximation (Fig. 5.1b) and Fresnel approximation (Fig. 5.1c), respectively. Overall, these images are similar. They show that Ochoa's approximation (proposed in this work) and Fresnel approximation (adopted by previous works [23, 36]) are effective for handling the propagation in the 1 mm pupil radius case.

However, the previous statement does not hold when a large (3 mm) pupil size is considered. Fig. 5.2 presents images of Airy disks generated for this case. These images were generated using the RS diffraction solution (Fig. 5.2a), Ochoa's approximation (Fig. 5.2b) and Fresnel approximation (Fig. 5.2c), respectively. The image obtained using the Fresnel approximation (Fig. 5.2c) differs considerably from the image obtained using the RS diffraction solution (Fig. 5.2a). On the other hand, the image obtained using the Ochoa's approximation (Fig. 5.2b) closely approximates the reference RS image (Fig. 5.2a). These observations indicated that the Fresnel approximation (adopted by previous works [23, 36]) may significantly underestimate the extent of the pattern for a relatively larger pupil size.

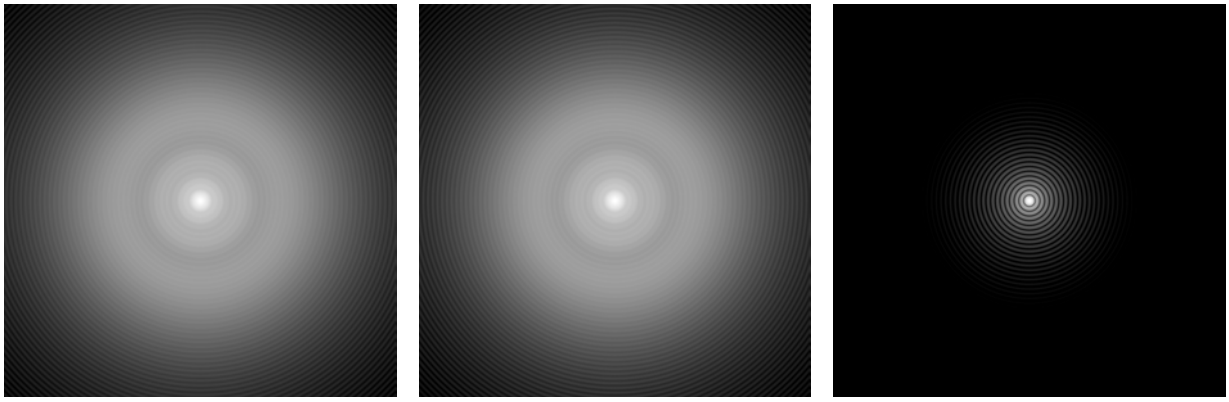

(a) (b) (c)

Figure 5.2: Airy patterns generated using different propagation algorithms and considering a 3 mm pupil radius. (a) Pattern obtained using RS diffraction solution. (b) Pattern obtained using Ochoa's approximation. (c) Pattern obtained using Fresnel approximation.

5.4 Starburst Pattern from Propagation Method

The previous section presented the Airy disks generated using different propagation methods and considering different pupil radii. In this section, we present results obtained considering obstacles, specifically particles, added to the lens as a mask. Starburst patterns depicted in Figs. 5.3a, 5.3b and 5.3c were generated using the RS diffraction solution, Ochoa's approximation and Fresnel approximation, respectively. As it can be observed by inspecting these results, the differences among the patterns generated using these different propagation methods were visually negligible when we considered a 1 mm pupil radius.

Starburst patterns shown in Figs. 5.3d, 5.3e and 5.3f were generated using the same propagation methods as Figs. 5.3a, 5.3b and 5.3c, respectively, but considering a 3 mm pupil radius. It can be observed that the pattern generated using the Fresnel approximation (Fig. 5.3f) significantly underestimated the extent of the pattern for a relatively larger pupil size. Nevertheless, one can still obtain a pattern that is suitable for computer graphics applications by increasing the intensity of the pattern with the cost of overexposing the centre area.

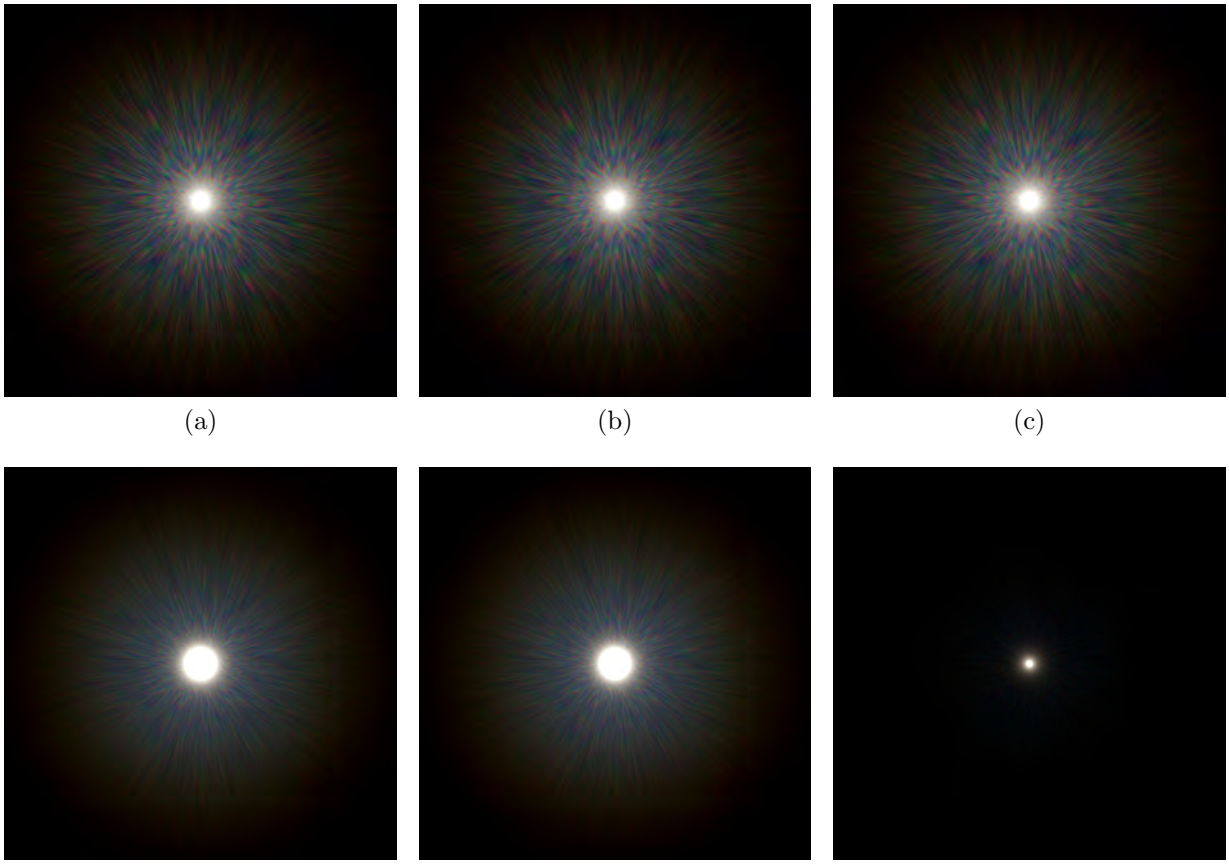

(a) (b) (c)

(d) (e) (f)

Figure 5.3: Starburst patterns generated using different propagation methods and considering different pupil radii. Left column: RS diffraction. Middle column: Ochoa's approximation. Right column: Fresnel approximation. Top row: 1 mm radius. Bottom row: 3 mm radius.

5.5 The Decay of the Energy in the Patterns

The dynamic range of the starburst pattern is relatively large. We compute the extent of the pattern by taking the average of the logarithm of the Y channel of cone stimulus on the circle with distance r to the focus point o as shown in the following expression:

$$f(r) = \frac{1}{2\pi r} \int_{|x-o|=r} \log_{10}(L_v(x))dx. \tag{5.2}$$

Using Eq. 5.2, we compute the extent of the patterns depicted in Fig. 5.3. Note that we manually shift the max of each curve to 0 to compare the decay rate effectively. The results presented in Fig. 5.4 show that the energy of the pattern decreases quickly along the radial direction as the energy is reduced by around five orders of magnitude when the distance is at 125 μm to the center. Meanwhile, we can quantitatively observe that the Fresnel approximation significantly underestimates the energy of the pattern when the pupil size is large as discussed in the last section.

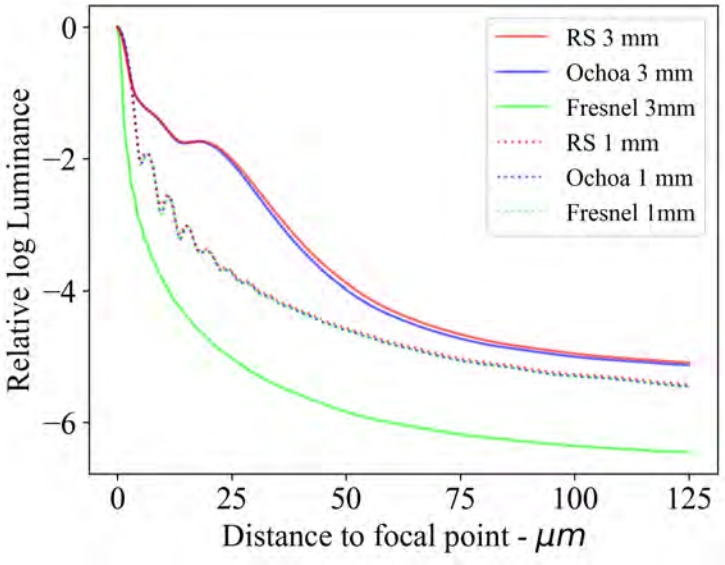

Figure 5.4: Average log luminance vs. distance plot for starburst patterns depicted in Fig. 5.3, computed using Eq. 5.2.

5.6 The Advantage of Chirp Z Transform

A crucial factor affecting the visual quality of the patterns is the physical size of the image plane, which corresponds to the number of pixels within the region of interest. Although the size ($N \times N$) of the matrix that represents the light wave stays constant during the

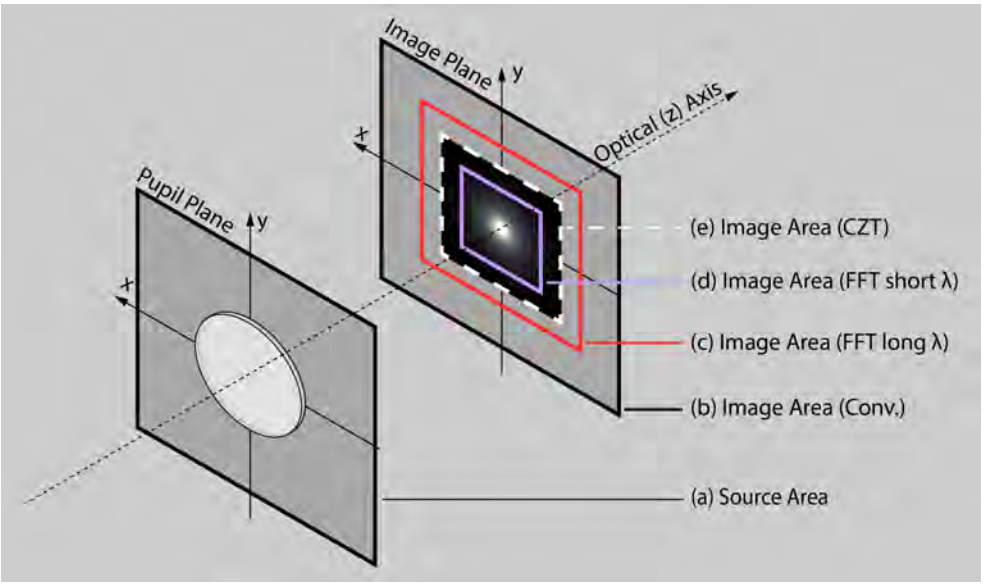

Figure 5.5: Diagram showing the variation in the physical size (in $\mu m \times \mu m$) of the square matrix ($N \times N$) used to represent the complex amplitude of the light wave on the pupil (image) plane. (a) Physical area on the pupil plane that corresponds to the matrix. (b) Physical area on the image plane after the propagation implemented with convolution. (c) Physical area on the image plane after the propagation of waves using an FFT implementation for long wavelengths. (d) Physical area on the image plane after the propagation using an FFT implementation for short wavelengths. (e) Physical area on the image plane after the propagation using CZT implementation.

propagation stage, its corresponding physical size (in $\mu m \times \mu m$) may change as shown in Fig. 5.5.

Such a variation in physical size can occur during the propagation stage implemented using different methods. With the convolution implementation (Section 3.3.1) of the RS diffraction solution, the physical size of the resulting matrix is always the same as the source matrix, regardless of the wavelength at which the light is being propagated [6]. However, this condition does not hold if FFT is directly applied to the pupil plane since the physical size of the resulting image plane is proportional to the wavelength [11]. The aforementioned change in physical size leads to the requirement of further scaling of the image plane so that the generated matrix can have the same physical size for all wavelengths (or resampling equivalently [23, 36]). Besides, the area of interest may only occupy a small portion of the resulting matrix. Those limitations induce extra computational costs and

possibly introduce errors during resampling. In comparison, CZT solves this problem as it allows users to select the region of interest (physical size of image plane) [13]. This feature, in turn, also enables the selection of the same physical size for all wavelengths.

Fig. 5.6 presents the results obtained for a 1 mm pupil radius using the Fresnel approximation and the FFT and CZT implementation methods. Overall, the results appear similar as expected, albeit the pattern obtained using FFT (Fig. 5.6a) is more blurred. Also, some aliasing can be observed between the rings of the patterns obtained using FFT (Fig. 5.6a, insets).

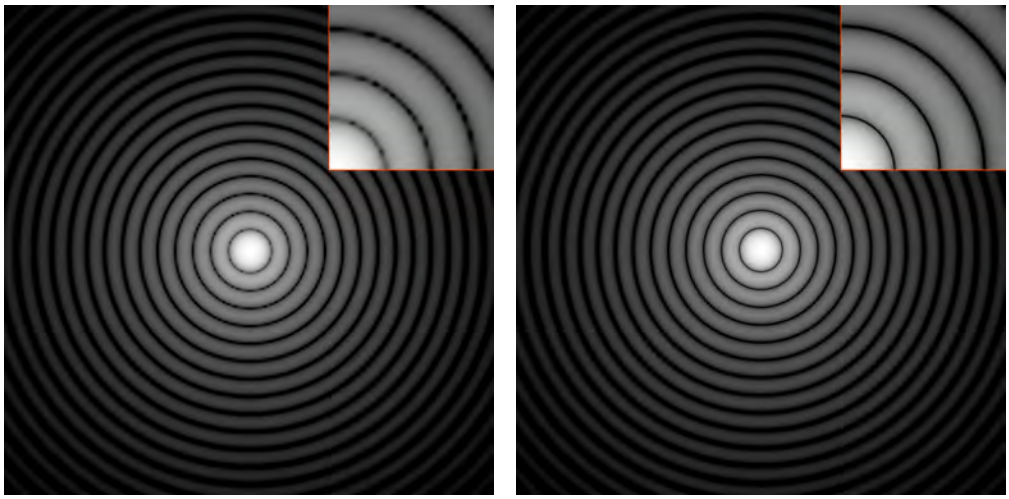

(a) (b)

Figure 5.6: Airy patterns generated for a 1 mm pupil radius using Fresnel approximation and different implementations methods. (a) Present pattern generated using FFT. (b) Present pattern generated using CZT. The insets in the top-right corners of each subfigure provide a zoom-in view of the central region.

5.7 Time and Space Efficiency

All propagation methods introduced in Section 3.3 and CZT were implemented using a constant number of FFT operations and their inverses. Thus, they all have time complexity $\mathcal{O}(N^2 log N^2)$ and space complexity $\mathcal{O}(N^2)$, where N is the number of rows of the square input matrix [13, 40]. We profile the performance of these algorithms considering distinct values for N and record the time consumption and peak memory usage in Table

5.1. Although the implementation affects the exact performance, the asymptotic trends of time and space match the theoretical complexities outlined earlier. Furthermore, as expected, the algorithms that employed FFT were faster than those that used CZT since CZT operations are implemented with two FFT operations and one inverse Fast Fourier transform (iFFT) operation.

Rayleigh-Sommerfeld diffraction with Fast Fourier transform			
Matrix Size	$Time_T$	$Time_R$	Memory Usage
16384	288.95s	233.86s	106.50 GB
Ochoa's approximation with Fast Fourier transform			
Matrix Size	$Time_T$	$Time_R$	Memory Usage
1024	0.08s	0.22s	0.17 GB
4096	2.83s	10.88s	2.69 GB
16384	46.34s	285.10s	43.02 GB
Fresnel diffraction with Fast Fourier transform			
Matrix Size	$Time_T$	$Time_R$	Memory Usage
1024	0.12s	0.22s	0.19 GB
4096	6.53s	10.94s	2.82 GB
16384	95.22s	286.42s	45.07 GB
Ochoa's approximation with Chirp Z transform			
Matrix Size	$Time_T$	$Time_R$	Memory Usage
1024	0.25s	N/A	0.27 GB
4096	8.96s	N/A	4.36 GB
16384	152.23s	N/A	69.65 GB
Fresnel diffraction with Chirp Z transform			
Matrix Size	$Time_T$	$Time_R$	Memory Usage
1024	0.27s	N/A	0.28 GB
4096	9.15s	N/A	4.35 GB
16384	157.45s	N/A	69.63 GB

Table 5.1: Time and peak memory costs. Matrix size refers to the size of the 2D matrix that represents waves. $Time_T$ is the time spent in executing of the propagation stage. $Time_R$ refers to the time to scale the propagation results to a specific size. This metric is only available for FFT implementations as CZT is capable of generating a matrix representing the image plane with a user-selected physical size. Memory usage corresponds to the peak usage during the whole execution procedure.

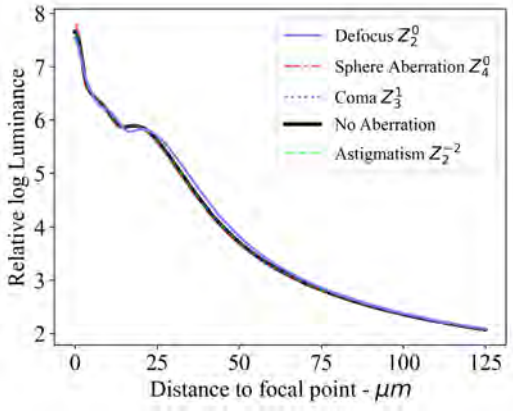

Figure 5.7: Average log luminance vs. distance plot for perfect focus (no aberration), defocus, primary astigmatism, primary coma and primary spherical aberration.

Note that when the input matrix size increases by a factor of 4 (from 4096 to 16384) in a Fresnel diffraction execution employing FFT, the memory usage increases by a factor of 16, growing from 2.82 GB to 45.07 GB. This is because the matrix size is a one-dimensional measure, whereas memory usage scales with two-dimension. Furthermore, we observe that with the FFT-based implementation, the Ochoa's approximation is approximately 6× faster than the reference solution, whereas the Fresnel approximation is only about 3× faster. This difference is mainly due to the fact that the Fresnel approximation formula (Eq. 3.11) contains a coefficient whose computation requires a markedly larger number of floating point operations than that of the Ochoa's approximation (Eq. 3.5).

It is also worth mentioning that Ochoa's approximation produces results that approximate the reference patterns (obtained using the RS diffraction solution) more closely than those produced by the Fresnel approximation. Moreover, the computational time associated with the Ochoa's approximation is lower than that associated with the Fresnel approximation. For these reasons, we suggest the use of the Ochoa's approximation, instead of the Fresnel approximation, in the generation of the starburst patterns discussed in this work.

5.8 Aberration Influence

As the aberration is believed to be a factor affecting the starburst phenomenon [28], we add distinct forms of aberration into the lens as part of our simulations. Specifically, we add defocus aberration Z_2^0, primary astigmatism Z_2^{-2}, primary coma aberration Z_3^1 and

primary spherical aberration Z_4^0 into the lens, with coefficients equal to -2.2, -0.125, -0.4 and -0.2, respectively, which were provided by Kong et al. [20]. Lastly, the radius of the pupil is set to 3 mm and the radius of aberration is assumed to be 5 mm according to the size of the lens. The aberrations are represented with Zernike polynomials with OSA/ANSI indexing scheme [29].

Using Eq. 5.2, we compute the extent of the patterns affected by the different aberrations. The results presented in Fig. 5.7 show that, under our setup, primary astigmatism, primary coma and primary spherical aberration do not obviously extend the extent of the pattern. Defocus, also known as myopia and hyperopia [22], has a more substantial effect, notably as a shift up of curves in the non-center area.

Chapter 6

Practical Ramifications

For the propagation stage, we assessed the generated starburst patterns (described by the PSF) by comparing them with the baseline patterns generated using the RS diffraction solution. However, we are not able to quantitatively evaluate the results obtained through the response stage (Section 4.3) since, to the best of our knowledge, there is no current technology capable of capturing the exact starburst pattern as seen by human observers. Please refer to Appendix B for examples illustrating the limitations of camera imaging systems with respect to the photographic capture of starburst patterns. Hence, we elected to qualitatively examine the visual simulation results obtained for different illumination conditions. We note that all patterns depicted in this chapter were generated using Ochoa's approximation (Section 3.3.2) and CZT implementation (Section 3.3.5).

6.1 Different Light Sources

Simpson [42] has mentioned that glare-related patterns seen under monochromatic light are different from those seen under white light as they break up into a large number of spots. Furthermore, van den Berg et al. [45] have stated that the radiating line in the chromatic PSF (*e.g.*, Figs. 6.1a and 6.1b) arises from the alignment of spots in each monochromatic PSF (*e.g.*, Fig. 6.1d) for different wavelengths. Thus, for our simulations, we selected four types of light sources based on their spectral power distributions (SPDs):

- light source with uniform SPD as the base case,
- standard illuminant D65 [16], which has smooth SPD,

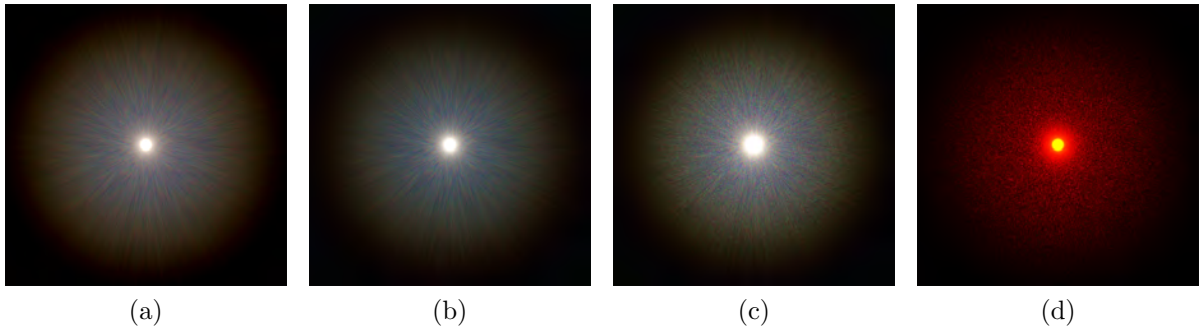

(a) (b) (c) (d)

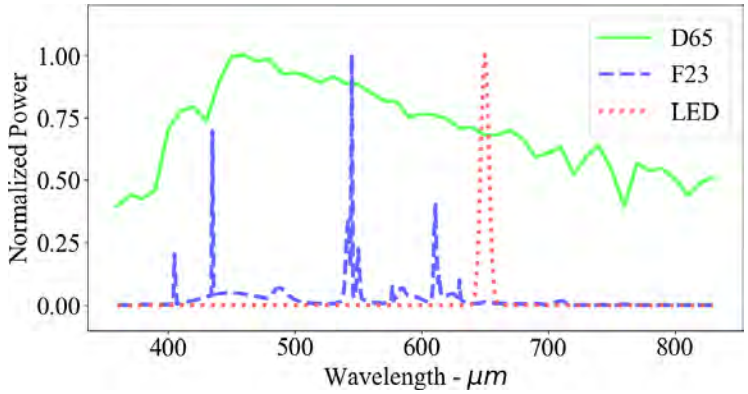

(e)

Figure 6.1: Starburst patterns generated using the proposed framework and considering different light sources. (a) Light source with uniform SPD. (b) CIE D65 illuminant. (c) CIE Fluorescent lamp (F23). (d) Red LED approximated with Gaussian distribution ($\mu = 650\ nm, \sigma = 20\ nm$). (e) Relative spectral power distributions of the light sources used in (b) [16], (c) [15] and (d). From (a) to (d), the SPDs of the light sources shift to a peak distribution from a smooth distribution, and the corresponding pattern shifts to discrete dots from spikes.

- CIE fluorescent lamp #23, which contains a few peaks in its SPD, and
- red light-emitting diode (LED) light whose SPD consists of a single peak.

As it can be observed in Fig. 6.1, the pattern obtained using the D65 illuminant has similar spikes as the pattern obtained considering the light source with uniform SPD, but a different colour. In contrast, the pattern obtained considering the fluorescent lamp fails

to form a spike in its PSF since its SPD consists of only a few peaks. Further, the pattern obtained using the red LED consists of discrete red dots since the SPD of the red LED only has a single peak.

6.2 The Role of Background Luminance

Previous works usually pay attention to the light source and overlook the background luminance around the light source. The results presented in Fig. 6.2 show that as the background luminance increases, the pattern generated by the light source gradually disappears. In Fig. 6.3, we set the reference black equal to the background luminance so that we can extract the pure starburst patterns depicted in Fig. 6.2. Therefore, to make a starburst pattern noticeable, the intensity of the light source should be significantly greater than the background illumination. Such a behaviour could be attributed to both the luminance distribution of the pattern (PSF) and the perception threshold (Section 3.4.3). Inspecting the curves depicted in Fig. 5.4, one can notice that the luminance drops exponentially as the distance from the center increases.

Moreover, as discussed in Section 3.4.3, the perception threshold requires a certain amount of additional stimulus from the pattern so that the patterns can appear to human observers. Human observers can see a pattern only if the light source is bright enough. This can happen when the energy associated with the outer part of a spike in the PSF, which has much smaller energy than the center, can induce sufficient stimulus to surpass the perception threshold for a given background.

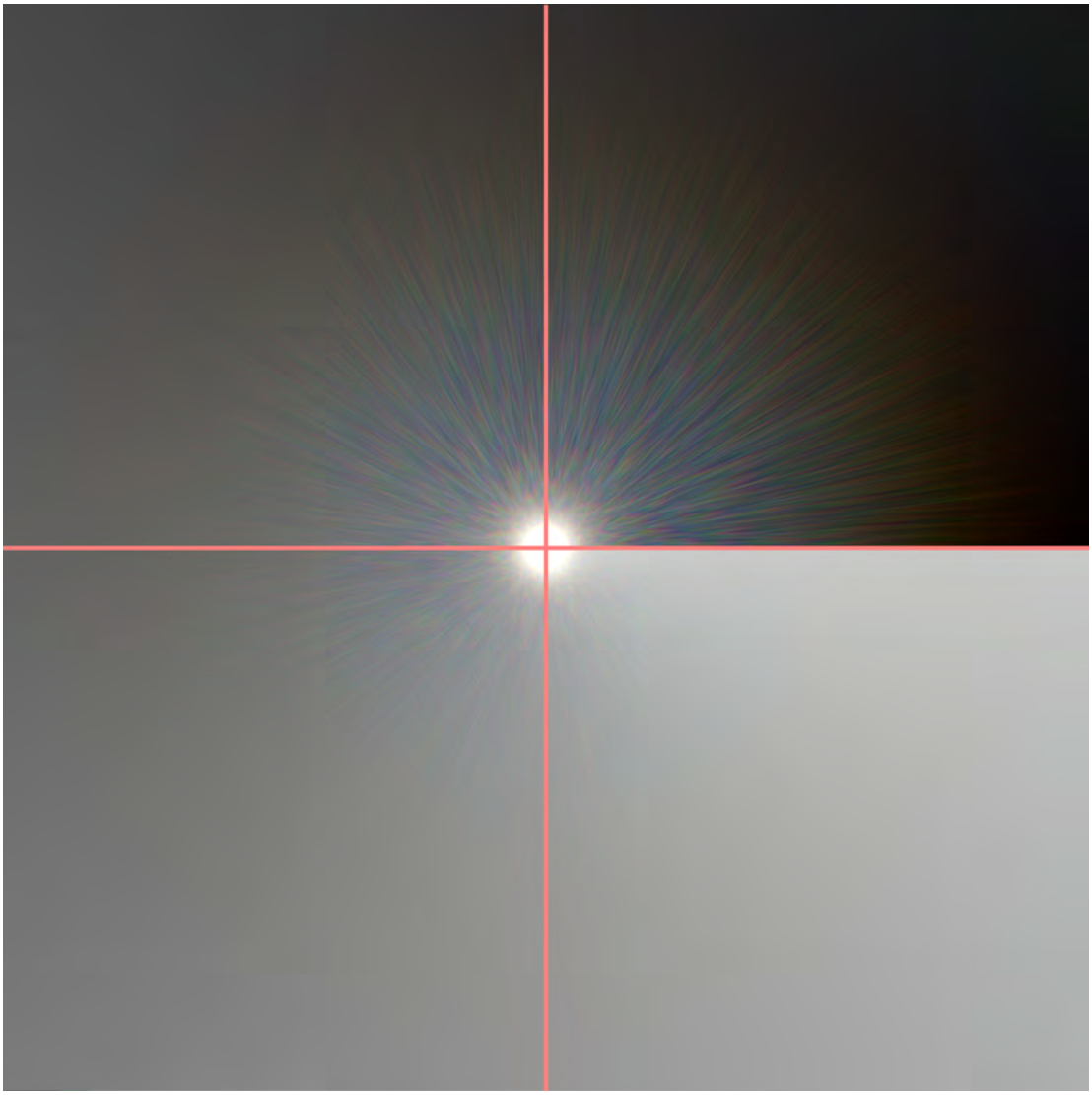

Figure 6.2: A sequence of images illustrating the effects of background luminance variation. As the luminance of the background light increases from the first quadrant (top right) going counter-clockwise, the pattern begins to dissolve into the background. The rationale is that the threshold for incremental brightness level is increasing as the background luminance increases, thus the noticeable pattern shrinks as the background luminance increases.

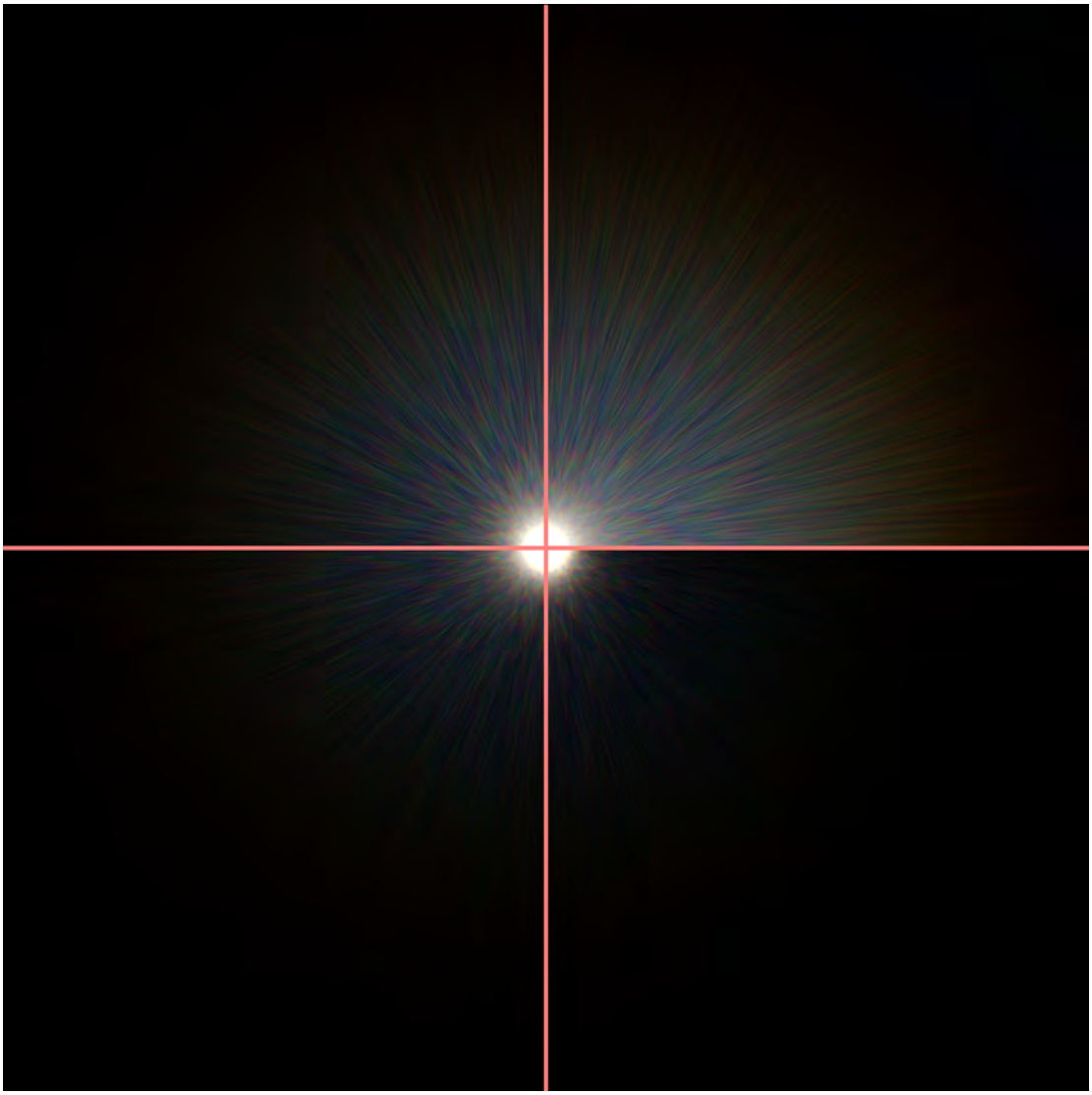

Figure 6.3: A sequence of images illustrating respectively showing pure versions of the starburst patterns depicted in Fig. 6.2. Images were obtained by setting reference black to the luminance of the background.

6.3 The Effect of Overall Luminance

The previous section addressed relative luminance requirements for the starburst pattern to be noticeable. It is important to note, however, that the absolute luminance and the state of photoreceptor cells also affect the visual appearance of the pattern. We remark that, for scenes with a relatively high illumination intensity, the cone responses are dominant, while for scenes with relatively low illumination intensity, the rod responses are dominant (Section 3.4.2).

We selected four cases to illustrate this aspect. Fig. 6.4a depicts relatively high-intensity light from both the light source and the background illumination. Since cones have a dominant role in this case, the resulting pattern is colourful. Fig. 6.4b, which depicts a rod-dominated case, has an opposite illumination setting of Fig. 6.4a, resulting in a pattern with an achromatic appearance. Fig. 6.4c depicts an illumination arrangement intermediate between the two previous cases. Lastly, Fig. 6.4d depicts a case in which the light source appears suddenly (*e.g.*, when a car makes a sharp turn in a corner and enters an observer's field of view). In this situation, the observer's rods are saturated and the cones are at a lower sensitivity state.

6.4 Rendering Applications

We render two distinct scenes (presented in Figs. 6.5 and 6.6) to illustrate the plausible depiction of the starburst phenomenon in different scenarios as well as visual enhancements brought about by the proposed framework with respect to previous works. The patterns are incorporated into the scenes by directly placing them around the light sources. Note that this operation is executed before applying tone mapping and before applying our proposed response function (Section 4.3, Eq. 4.10).

As mentioned in Section 1, driving is a classic scenario for human observers to see the starburst pattern. Figs. 6.5a and 6.5b depict examples of the patterns observed around car headlights at night, while Figs. 6.6a and 6.6b depict examples that can be observed at the spots where the specular reflection of sunlight takes place during daytime. Besides that, patterns in the nighttime scene and daytime scene were generated considering 3 mm and 1 mm pupil radii, respectively.

The results generated using our proposed response function are presented in Figs. 6.5b and 6.6b. Results obtained using the Narkowicz's fitted ACES tone mappings curve, which

has been used in the entertainment industry (Unreal and Unity) [26], are presented in Figs. 6.5a and 6.6a.

The scene illustrated by Fig. 6.5a depicts patterns obtained considering cone-dominated responses (*e.g.*, as illustrated in Fig. 6.4a) like the previous works [23, 36] have done for both daytime and nighttime scenes. By considering a mixed illumination setting, with both cones and rods providing considerable contributions (*e.g.*, as illustrated in Fig. 6.4c), the patterns generated using our proposed response function, presented in Fig. 6.5b, show a low-saturation colour and a fade-out transition into the background. Note that the scene depicted in Fig. 6.5b looks less colourful than the one depicted in Fig. 6.5a. This may be attributed to the role played by the rod cells [32] which is taken into account in the proposed framework.

Turning to the daytime scenes, we note that the patterns' visibility is affected by the local background luminance in both Figs. 6.6a and 6.6b. The patterns are more noticeable around the darker regions (*e.g.*, indoors, car tires and car interiors) and less noticeable around the brighter regions (*e.g.*, the sky and body of the car).

It can be observed in Figs. 6.5a and 6.6a that the selected tone mapping algorithm makes the spikes appear more discernible from their surroundings. This aspect is not consistent with the patterns perceived by an average human observer. In those patterns, some of the spike details (associated with the contrast between them and the background) are washed out by the background luminance (Section 6.2). By using the proposed response function, we can obtain depictions of the starburst patterns (Figs. 6.5b and 6.6b) that are closer to those perceived by human observers.

Note that the overall visual depiction of starburst patterns results from multiple factors, including the scene illumination level and the distinct photoreceptor sensitivities, with the rods taking seconds to restore their sensitivity instead of minutes taken by the cones (Section 3.4.4). We also remark that each person may see different patterns due to the eye structure diversity. As a result, besides typical graphics applications, we aim to employ the proposed framework to allow individuals to assess their own perception of starburst patterns through the modification of simulation parameters. Accordingly, related aspects are addressed in the next chapter.

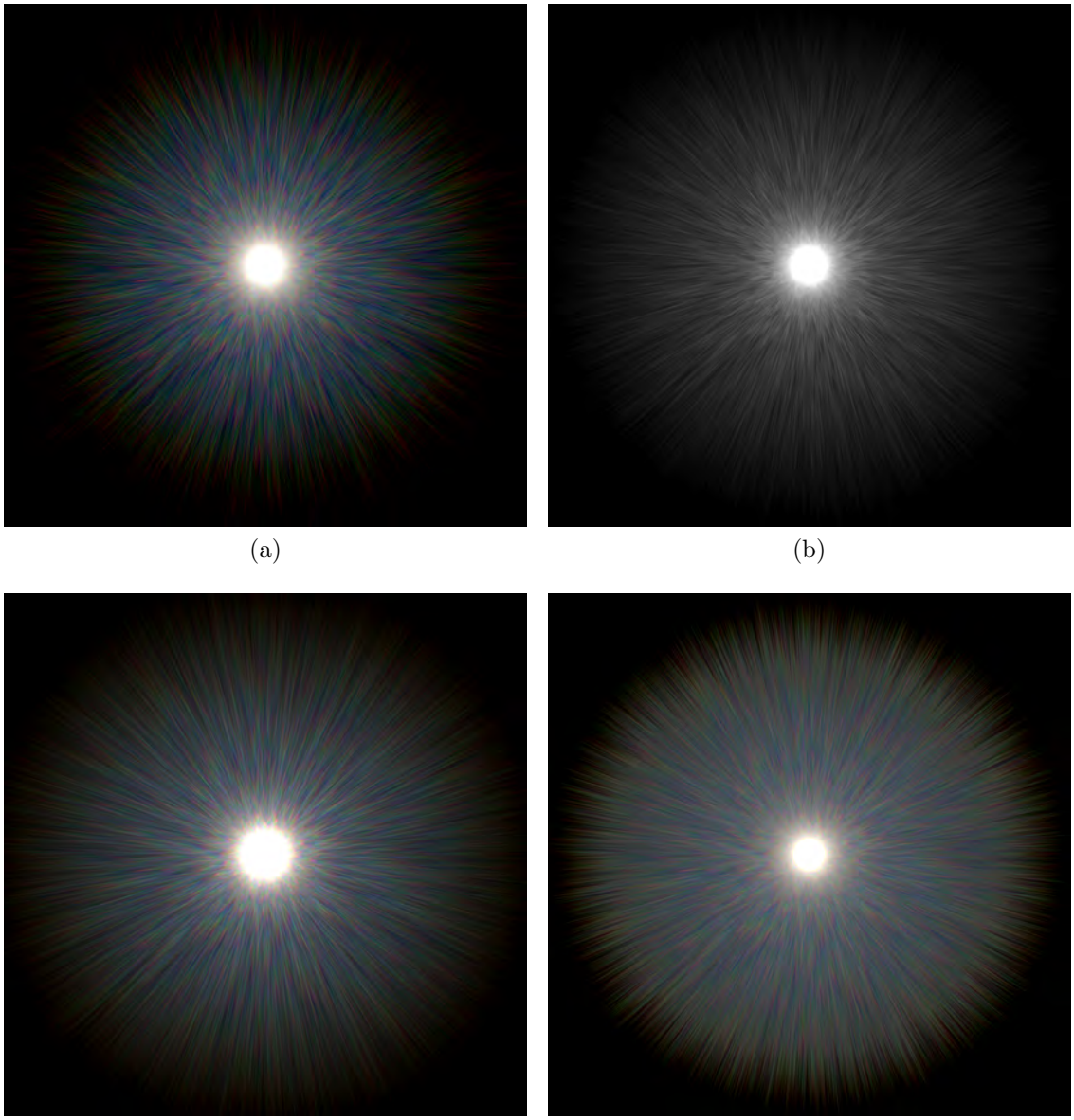

(a) (b)

(c) (d)

Figure 6.4: Images showing a starburst pattern under different illumination conditions. (a) Depicts a scene with high light source and background intensities. (b) Depicts a scene with low light source and background intensities. (c) Presents the result of mixing (a) and (b). (d) Depicts the scene with rod saturation and low cone sensitivity.

(a)

(b)

Figure 6.5: Images depicting the incorporation of starburst patterns (around the car headlights) into a nighttime scene. (a) The colour and intensity of the patterns and their surrounding background are adjusted using the Narkowicz's fitted ACES tone mapping curve [26]. (b) The colour and intensity of the patterns and their surrounding background are adjusted through the response stage of the proposed framework.

(a)

(b)

Figure 6.6: Images depicting the incorporation of starburst patterns (around the car's specular highlights) into a daytime scene. (a) The colour and intensity of the patterns and their surrounding background are adjusted using the Narkowicz's fitted ACES tone mapping curve [26]. (b) The colour and intensity of the patterns and their surrounding background are adjusted through the response stage of the proposed framework.

Chapter 7

Starburst Simulation Insights

Based on the outcomes of our simulations, we derived a few biophysical insights about the inner workings of the starburst phenomenon. These insights are outlined in the following sections. We bring forward these insights so that they can be further explored through actual experiments once the necessary technology becomes available.

7.1 Light Source Intensity

In Chapter 1, we described the starburst phenomenon as the event resulting from the process by which human observers perceive the starburst patterns around a bright light source with their naked eye. Recall that the observation consists of two parts - stimulated (propagation) and noticed (response). There are no restrictions on the light source. Theoretically, both primary and secondary light sources could induce a stimulus with a starburst shape on the retina due to the diffraction caused by the particles in the eyeball. However, only the stimulus from light sources that are significantly more intense than their surroundings, as described in Section 6.2, are finally noticeable to humans.

7.2 Aberration and Pupil Size

Reinstein et al. [35] point out that the frequency of the occurrence of the starburst phenomenon shows a positive correlation with aberrations and pupil size in dark environments. To simulate the pattern considering different pupil sizes in the dark environment, we set

the intensity of the light to be much stronger than the background, but kept the overall illumination level low. In addition, to simulate the dilation of the pupil while keeping all other parameters fixed, we double the intensity of the light source and background associated with the patterns depicted in Fig. 7.1a to obtain the pattern depicted in Fig. 7.1b. We then further double the light source and background intensities to obtain the pattern depicted in Fig. 7.1c. The sequences of images presented in Fig. 7.1 show that more incoming light flux leads to a larger spread of the pattern. This aligns with the effects elicited by a reducing pupil size, which, according to Xu et al. [47], mitigates the phenomenon.

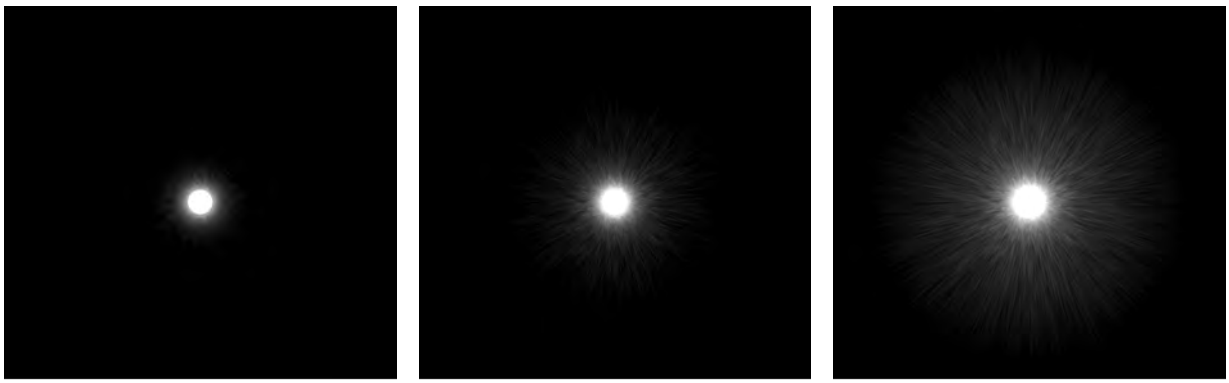

(a) (b) (c)

Figure 7.1: Images illustrating how pupil size affects the luminous flux and size of the pattern. (a) The pattern obtained by considering that both the light source and the background illumination have low intensities. (b) The pattern obtained by considering that both the light source and the background illumination have intensities doubled relative to the setup in (a). (c) The pattern obtained by considering that both the light source and the background illumination have intensities doubled relative to the setup in (b).

As discussed in Section 5.8, aberrations on the lens (except defocus) do not significantly affect the extent of the starburst patterns. This seems in contradiction with the positive correlation mentioned by Reinstein et al. [35]. We note that the human lens is under serious aberrations when the pupil is larger [20]. Therefore, one possibility is that the dilation of the pupil causes a human observer to be easily affected by the starburst phenomenon as discussed earlier. Meanwhile, an eyeball with a dilated pupil also exhibits more aberrations. That may explain the positive correlation between the frequency of starburst symptoms and aberrations, while solely aberrations (except defocus) do not make the pattern larger.

Mainster et al. [24] have mentioned that aberrations only determine the central 0.1

degrees of PSF (around 35 μm of radius on the retina if the propagation distance is 20 mm), while the extent of the starburst patterns is much larger than that as shown in Section 5.8. Our simulations, on the other hand, suggest that aberrations have a minor impact on the starburst phenomenon.

7.3 Postsurgical Effects

It has been reported that eye surgery patients tend to be more susceptible to glare phenomena, including starbursts [8, 33, 35]. We believe that this situation may be associated with the pupil dilation after the surgical procedures.

Chapter 8

Conclusion and Future Work

This thesis described a modular framework proposed for the plausible reproduction of the starburst phenomenon. We employed the Rayleigh-Sommerfeld (RS) diffraction solution and its Ochoa's approximation. To the best of our knowledge, these algorithms have not been used in similar computer graphics applications before. They are capable of enhancing the physical correctness compared to Fresnel and Fraunhofer approximations adopted in previous works [18, 23, 36]. Besides that, replacing the Fast Fourier transform (FFT) by the Chirp Z transform (CZT) in the implementation of these approximations allows for a further increase in the visual resolution of the generated patterns. By considering specific characteristics of the human visual system (HVS) [9], background luminance and spectral distribution of the light source, the proposed framework can be employed to generate plausible depictions of the starburst phenomenon for distinct illumination scenarios.

As future work, we intend to consider other biological structures (*e.g.*, eyelash and lens grating) that may also affect the diffraction of light reaching the retina. Furthermore, we plan to explore the use of the vector diffraction theory [11] to further increase the physical correctness of our simulations by properly accounting for eye microstructures (*e.g.*, particles) that have a size (less than 10 μm [42]) comparable to the wavelength of the incoming light. We also intend to investigate alternatives to enhance the mapping operator employed in the response stage of the proposed framework.

Lastly, we remark that the plausible reproduction of the starburst phenomenon is also of interest to other fields of study such as applied optics, psychology, ophthalmology and colourimetry, just to name a few. Viewed in this context, we believe that the investigation described in this thesis may also serve as a catalyst for future synergistic collaborations among researchers from those fields and computer science.

References

[1] ASTM. Standard Terminology of Appearance. Technical Report E284-17, ASTM (American Society for Testing and Materials), International, West Conshohocken, PA, USA, 2017. doi: 10.1520/E0284-22.

[2] D. A. Atchison and L. N. Thibos. Optical models of the human eye. *Clinical and Experimental Optometry*, 99(2):99–106, Mar. 2016.

[3] F. Banterle, A. Artusi, T. O. Aydin, P. Didyk, E. Eisemann, D. Gutierrez, R. Mantiuk, and K. Myszkowski. Multidimensional image retargeting. In *SIGGRAPH Asia 2011 Courses*, pages 1–612, Hong Kong China, Dec. 2011. ACM.

[4] F. Banterle, A. Artusi, K. Debattista, and A. Chalmers. *Advanced High Dynamic Range Imaging*. Taylor & Francis, CRC Press, Boca Raton, second edition, 2018.

[5] L. Bluestein. A linear filtering approach to the computation of discrete Fourier transform. *IEEE Transactions on Audio and Electroacoustics*, 18(4):451–455, Dec. 1970.

[6] D. Claus and J. M. Rodenburg. Pixel size adjustment in coherent diffractive imaging within the Rayleigh–Sommerfeld regime. *Applied Optics*, 54(8):1936, Mar. 2015.

[7] O. Cornut. Dear ImGui, 2024. Published: GitHub repository.

[8] N. I. Fan-Paul, J. Li, J. S. Miller, and G. J. Florakis. Night vision disturbances after corneal refractive surgery. *Survey of Ophthalmology*, 47(6):533–546, Nov. 2002.

[9] J. A. Ferwerda, S. N. Pattanaik, P. Shirley, and D. P. Greenberg. A model of visual adaptation for realistic image synthesis. In *Proceedings of the 23rd Annual Conference on Computer Graphics and Interactive Techniques*, pages 249–258. ACM, Aug. 1996.

[10] A. S. Glassner. *Principles of Digital Image Synthesis*. Morgan Kaufmann, San Francisco, Calif, second edition, 2004.

[11] J. W. Goodman. *Introduction to Fourier Optics*. W.H. Freeman, Macmillan Learning, New York, fourth edition, 2017.

[12] W. N. Grimes, A. Songco-Aguas, and F. Rieke. Parallel processing of rod and cone signals: retinal function and human perception. *Annual Review of Vision Science*, 4(1):123–141, Sept. 2018.

[13] Y. Hu, Z. Wang, X. Wang, S. Ji, C. Zhang, J. Li, W. Zhu, D. Wu, and J. Chu. Efficient full-path optical calculation of scalar and vector diffraction using the Bluestein method. *Light: Science & Applications*, 9(1):119, July 2020.

[14] M. Hullin, E. Eisemann, H.-P. Seidel, and S. Lee. Physically-based real-time lens flare rendering. In *ACM SIGGRAPH 2011*, pages 1–10, Vancouver British Columbia Canada, July 2011. ACM.

[15] International Commission On Illumination (CIE). Relative spectral power distributions of illuminants representing typical fluorescent lamps, 1nm wavelength steps. Technical Report CIE 2018, Vienna, Austria, 2018.

[16] International Commission On Illumination (CIE). CIE standard illuminant D65. Technical Report CIE 2022, Vienna, Austria, 2022.

[17] F. Kainz, R. Bogart, and D. Hess. The OpenEXR image file format. *ACM SIGGRAPH Technical Sketches*, 2, 2003.

[18] M. Kakimoto, K. Matsuoka, T. Nishita, T. Naemura, and H. Harashima. Glare generation based on wave optics. In *12th Pacific Conference on Computer Graphics and Applications, 2004. PG 2004. Proceedings.*, pages 133–142, Seoul, Korea, 2004. IEEE.

[19] J. M. Kessenich, G. Sellers, and D. Shreiner. *OpenGL programming guide: the official guide to learning OpenGL, version 4.5 with SPIR-V*. Addison-Wesley, Boston, MA, ninth edition edition, 2017.

[20] M.-m. Kong, Z.-s. Gao, X.-h. Li, S.-h. Ding, X.-m. Qu, and M.-q. Yu. A generic eye model by reverse building based on Chinese population. *Optics Express*, 17(16):13283, Aug. 2009.

[21] M. Lendermann, J. S. Q. Tan, J. M. Koh, and K. H. Cheong. Computational imaging prediction of starburst-effect diffraction spikes. *Scientific Reports*, 8(1):16919, Nov. 2018.

[22] M. Lombardo and G. Lombardo. Wave aberration of human eyes and new descriptors of image optical quality and visual performance. *Journal of Cataract and Refractive Surgery*, 36(2):313–331, Feb. 2010.

[23] L. R. Luidolt, M. Wimmer, and K. Krosl. Gaze-dependent simulation of light perception in virtual reality. *IEEE Transactions on Visualization and Computer Graphics*, 26(12):3557–3567, Dec. 2020.

[24] M. A. Mainster and P. L. Turner. Glare's causes, consequences, and clinical challenges after a century of ophthalmic study. *American Journal of Ophthalmology*, 153(4):587–593, Apr. 2012.

[25] H. Maître. *From photon to pixel: the digital camera handbook*. Digital signal and image processing series. John Wiley & Sons, Inc, Hoboken, NJ, 2015.

[26] T. Möller, E. Haines, and N. Hoffman. *Real-Time Rendering*. CRC Press, Taylor and Francis Group, Boca Raton, fourth edition, 2018.

[27] E. Nakamae, K. Kaneda, T. Okamoto, and T. Nishita. A lighting model aiming at drive simulators. *ACM SIGGRAPH Computer Graphics*, 24(4):395–404, Sept. 1990.

[28] R. Navarro and M. Angeles Losada. Shape of stars and optical quality of the human eye. *Journal of the Optical Society of America A*, 14(2):353, Feb. 1997.

[29] K. Niu and C. Tian. Zernike polynomials and their applications. *Journal of Optics*, 24(12):123001, Dec. 2022.

[30] N. A. Ochoa. Alternative approach to evaluate the Rayleigh-Sommerfeld diffraction integrals using tilted spherical waves. *Optics Express*, 25(10):12008, May 2017.

[31] Y. Ohno, T. Goodman, P. Blattner, J. Schanda, H. Shitomi, A. Sperling, and J. Zwinkels. Principles Governing Photometry (2nd edition). *Metrologia*, 57(2):020401, Apr. 2020.

[32] S. N. Pattanaik, J. A. Ferwerda, M. D. Fairchild, and D. P. Greenberg. A multiscale model of adaptation and spatial vision for realistic image display. In *Proceedings of the 25th Annual Conference on Computer Graphics and Interactive Techniques - SIGGRAPH '98*, pages 287–298. ACM Press, 1998.

[33] A. Pusnik, G. Petrovski, and X. Lumi. Dysphotopsias or unwanted visual phenomena after cataract surgery. *Life*, 13(1):53, Dec. 2022.

[34] A. Reichenbach and A. Bringmann. Retina: neuroanatomy and physiology. In D. W. Pfaff, N. D. Volkow, and J. L. Rubenstein, editors, *Neuroscience in the 21st Century*, pages 955–1027. Springer International Publishing, Cham, 2022.

[35] D. Z. Reinstein, T. J. Archer, R. S. Vida, G. I. Carp, J. F. R. Reinstein, and C. McAlinden. Objective and subjective quality of vision after SMILE for high myopia and astigmatism. *Journal of Refractive Surgery*, 38(7):404–413, July 2022.

[36] T. Ritschel, M. Ihrke, J. R. Frisvad, J. Coppens, K. Myszkowski, and H. Seidel. Temporal glare: real-time dynamic simulation of the scattering in the human eye. *Computer Graphics Forum*, 28(2):183–192, Apr. 2009.

[37] P. Rokita. A model for rendering high intensity lights. *Computers & Graphics*, 17(4):431–437, July 1993.

[38] J. Rubinstein. On the geometry of visual starbursts. *Journal of the Optical Society of America A*, 36(4):B58, Apr. 2019.

[39] L. M. Sanchez-Brea, A. Soria-Garcia, J. Andres-Porras, V. Pastor-Villarrubia, M. H. Elshorbagy, J. Del Hoyo, F. J. Torcal-Milla, and J. Alda. Diffractio: an open-source library for diffraction and interference calculations. In P. J. De Groot, P. Picart, and F. Guzman, editors, *Optics and Photonics for Advanced Dimensional Metrology III*, page 46, Strasbourg, France, June 2024. SPIE.

[40] F. Shen and A. Wang. Fast-Fourier-transform based numerical integration method for the Rayleigh-Sommerfeld diffraction formula. *Applied Optics*, 45(6):1102, Feb. 2006.

[41] M. Shinya, T. Saito, and T. Takahashi. Rendering techniques for transparent objects. *Proceedings of Graphics Interface '89*, London, 1989.

[42] G. C. Simpson. Ocular haloes and coronas. *British Journal of Ophthalmology*, 37(8):450–486, Aug. 1953.

[43] G. Spencer, P. Shirley, K. Zimmerman, and D. P. Greenberg. Physically-based glare effects for digital images. In *Proceedings of the 22nd Annual Conference on Computer Graphics and Interactive Techniques - SIGGRAPH '95*, pages 325–334. ACM Press, 1995.

[44] J. Tumblin and H. Rushmeier. Tone reproduction for realistic images. *IEEE Computer Graphics and Applications*, 13(6):42–48, Nov. 1993.

[45] T. J. T. P. Van Den Berg, M. P. J. Hagenouw, and J. E. Coppens. The ciliary corona: physical model and simulation of the fine needles radiating from point light sources. *Investigative Opthalmology & Visual Science*, 46(7):2627, July 2005.

[46] G. Ward. A contrast-based scalefactor for luminance display. In *Graphics Gems IV*, pages 415–421. Academic Press Professional, Inc., 1994.

[47] R. Xu, P. Kollbaum, L. Thibos, N. Lopez-Gil, and A. Bradley. Reducing starbursts in highly aberrated eyes with pupil miosis. *Ophthalmic and Physiological Optics*, 38(1):26–36, 2018.

[48] R. Xu, L. N. Thibos, N. Lopez-Gil, P. Kollbaum, and A. Bradley. Psychophysical study of the optical origin of starbursts. *Journal of the Optical Society of America A*, 36(4):B97, Apr. 2019.

[49] Y.-r. Yang, J. Wanek, and M. Shahidi. Representing the retinal line spread shape with mathematical functions. *Journal of Zhejiang University SCIENCE B*, 9(12):996–1002, Dec. 2008.

APPENDICES

Appendix A

Brightness Mapping Function

In this appendix, we derive the luminance to brightness mapping function introduced in Section 4.4.

Initially, we denote the luminance assigned to reference white (255) and the luminance assigned to reference black (0) by $L^{refWhite}$ and $L^{refBlack}$, respectively. We then employ L^{env} to denote the luminance of the environment. Lastly, we use $L^{pattern}_{photopic}$ and $L^{pattern}_{scotopic}$ to denote the patterns' photopic luminance (associated with the cones) and scotopic luminance (associated with the rods), respectively.

The brightness values assigned to reference white, reference black and the combination of pattern and environment stimuli are calculated using the following expressions:

$$B^{refWhite} = B(L^{refWhite}, L^{refWhite}), \tag{A.1}$$

$$B^{refBlack} = B(L^{refBlack}, L^{refBlack}), \tag{A.2}$$

and

$$B^{pattern+evn} = B(L^{pattern}_{photopic} + L^{env}, L^{pattern}_{scotopic} + L^{env}), \tag{A.3}$$

where the function B represents the mapping from luminance to brightness (Eq. 4.7).

The colour c assigned to $B^{pattern+evn}$ is then defined through the following linear interpolation expression:

$$B^{pattern+evn} = B^{refBlack} + c(B^{refWhite} - B^{refBlack}), \tag{A.4}$$

which can be rewritten as:

$$\begin{aligned} c =& \frac{B^{pattern+evn} - B^{refBlack}}{B^{refWhite} - B^{refBlack}} \\ =& \frac{B(L^{pattern}_{photopic} + L^{env}, L^{pattern}_{scotopic} + L^{env}) - B(L^{refBlack}, L^{refBlack})}{B(L^{refWhite}, L^{refWhite}) - B(L^{refBlack}, L^{refBlack})}. \end{aligned} \tag{A.5}$$

Finally, Eq.4.8 can be obtained by applying Eq. A.5 for three colour channels:

$$c_{LMS}[i] = \frac{L^{pattern}_{photopic}[i] + L^{env}[i], L^{pattern}_{scotopic}[i] + L^{env}[i]) - B(L^{refBlack}[i], L^{refBlack}[i])}{B(L^{refWhite}[i], L^{refWhite}[i]) - B(L^{refBlack}[i], L^{refBlack}[i])}, \tag{A.6}$$

where LMS is the colour space that represents the response of three types of cones [4], with $i = 1, 2, 3$ representing each colour component. Note that, in the main body of this thesis, we added subscript v to each of the notations to emphasize that they are luminance in contrast to radiance. For formatting reasons, we also abbreviated $L^{pattern}_{photopic}$ and $L^{pattern}_{scotopic}$ to L^{p}_{v} and L^{s}_{v}, respectively.

Appendix B

Photographics Illustration of Starburst Scenarios

In this appendix, we present a sequence of photos depicting scenarios suitable for the perception of the starburst phenomenon. The photos were taken using a Sony ILCE7RM5 camera with a Tamron A063 lens.

In Fig. B.1, we present a sequence of photos depicting a nighttime scene. These photos were taken varying the following camera parameters:

- aperture ($f/\# = f/2.8, f/5.6, f/11, f/22$) and
- sensitivity ($ISO = 100, 320, 1250, 3200$).

The remaining parameters, focal length and exposure time, were kept as $f = 75\ mm$ and $t = 2.5s$, respectively.

In Fig. B.2, we present a sequence of photos depicting a daytime scene. These photos were taken varying the following camera parameters:

- aperture ($f/\# = f/2.8, f/5.6, f/11, f/22$),
- exposure time ($t = 1/1000s, 1/400s, 1/100s, 1/25s$) and
- sensitivity ($ISO = 100, 100, 125, 100$).

(a) (b)

(c) (d)

Figure B.1: A sequence of photos taken by a camera during nighttime to show the camera version of starburst patterns. The patterns could be observed around the headlights. (a), (b), (c) and (d) are with aperture sizes $f/\# = f/2.8, f/5.6, f/11$ and $f/22$, respectively.

The focal length was kept as $f = 75\ mm$.

Note that although some spikes can be observed in the photos presented in Figs. B.1 and B.2, the photographic depiction of the phenomenon cannot fully capture its visual richness as perceived by a human observer through the HVS. This limitation may be attributed to the presence of biological microstructures, which can diffract light, on the human crystalline lens [36]. The lens of a camera imaging system, on the other hand, has no structural irregularities under normal manufacturing conditions.

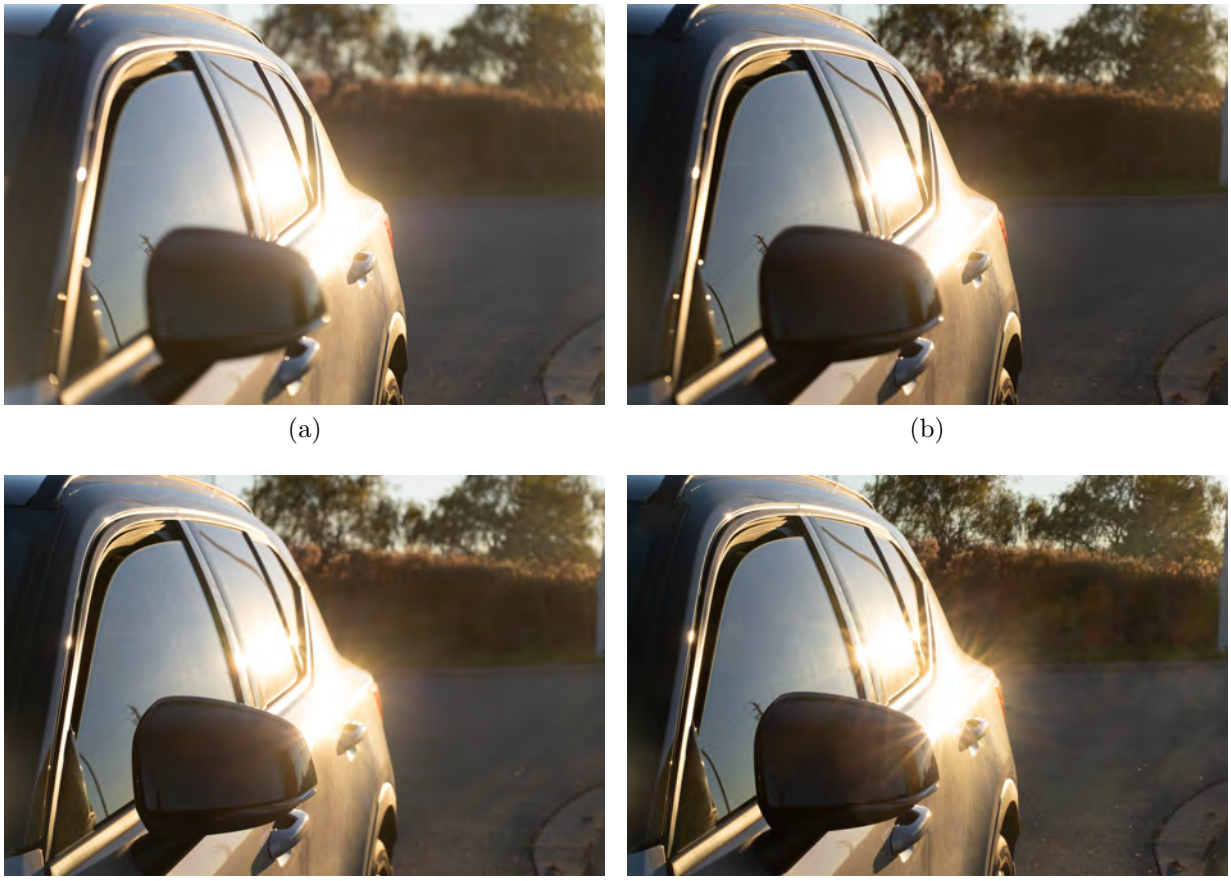

(a) (b)

(c) (d)

Figure B.2: A sequence of photos taken by a camera during daytime to show the camera version of starburst patterns. The patterns could be observed around the specular reflection spots. (a), (b), (c) and (d) are with aperture sizes $f/\# = f/2.8, f/5.6, f/11$ and $f/22$, respectively.

It is worth noting that the patterns observed on the photographs resulted from the diffraction occurred at the edge of the aperture in a camera lens system [14]. In our work, however, we simulate the patterns resulted from the diffraction caused by particles (representing biological microstructures) on the human crystalline lens [36]. Due to the distinct characteristics of the human eye and the camera's optical system (*e.g.,* lens with less imperfections), the latter cannot produce the same depictions of starburst patterns perceived by human observers. We note that these patterns contain more spikes than the

patterns captured in the photographs.

While the HVS has photosensitive cells, cones and rods, (digital) cameras use filters (*e.g.,* Bayer filter [25]) in conjunction with a CMOS (Complementary Metal Oxide Semiconductor) sensor [25] to convert light to colours. Such functionality is similar to the HVS's photopic sensitivity (associated with the cone cells). The lack of scotopic sensitivity (associated with rod cells) makes the camera unable to capture the correct colours of nighttime scenes. Also, the relatively limited dynamic range of the cameras prevents them from capturing all the spike details (associated with the contrast between the spikes and the background) of the starburst patterns. For example, if a camera sets its exposure based on the intensity of a light source, its limited dynamic range may underexpose dark areas, leading to a loss of these details. In this case, the spikes would appear unrealistically less discernible from their surroundings.

In short, the patterns observed in photos result from diffraction taking place at the edge of the aperture of a camera's lens system, while starburst patterns observed by the naked eye result from biological microstructures (particles) on the crystalline lens. Such differences hinder the evaluation of computer-generated depictions of starburst patterns through comparisons with photos attempting to capture them as they are perceived by a human observer.

Index of Terms